Length Scale Insensitive Phase-Field Fracture Methodology for Brittle and Ductile Materials

William Huber , Mohsen Asle Zaeem [*]

Department of Mechanical Engineering, Colorado School of Mines, CO 80401, USA

ARTICLE INFO

ABSTRACT

We present length scale insensitive phase-field fracture models for brittle and ductile fracture to address the deficiencies of widely implemented models which over-estimate crack dissipation. An approach is proposed to attain a regularization length scale insensitive mechanical response, which considers a continuous approximation of a crack boundary with a function of infinite support. This is in contrast to previous approaches to attain a length scale insensitive response which exploited approximations of the crack boundary with functions of finite support. The choice of these functions with finite support creates implementational challenges which are avoided in the presented quasi-brittle and ductile fracture models with infinite support of the phase-field. The capability of these models is demonstrated in several benchmarks with attention given to the sensitivity of the structural response with respect to the choice of regularization length scale. The models are validated against a three-point bending test on a concrete specimen and an in-plane shear test on a steel specimen.

1. Introduction

The ubiquity of damage and fracture as a failure mechanism in structural materials has attracted a great deal of attention from engineers and academics, giving rise to numerous theories and analyses of the phenomenon. The pioneering contributions of Griffith [1] and later Irwin [2] to the field of fracture mechanics have since been expanded and applied in computational techniques to assess the stability of cracked structures and to predict crack growth. These techniques include the extended finite element method [3] and remeshing techniques [4] to model a discontinuity. However, these techniques require external criteria to determine the nucleation site of a crack, the direction of crack propagation, and the propagation length of a crack. On the other hand, techniques from classical damage mechanics [5] consider discontinuities in the displacement field to be smeared (typically over the length of a finite element) and do not require external criteria to determine how a discontinuity should propagate. Without gradient enhancement, these approaches suffer from mesh dependence, especially in cases with curved crack paths [6]. While no single approach has become dominant in the field of computational fracture mechanics, the focus of the present investigation is the phase-field fracture method, an alternative technique which may rectify the issues of the aforementioned approaches.

The phase-field fracture method builds its foundation on Francfort and Marigo's [7] variational formulation of Griffith's brittle fracture theory and Bourdin's [8] numerical approach mentioned therein. Bourdin's [8] phase-field approach is based on the concept of Γ – convergence in which a smeared crack energy functional converges to that of the discrete case as the width (referred to as the characteristic damage scale) of the smeared crack zone decreases. In the phase-field approach, the smeared crack is represented with an order parameter (the phase-field) which, together with an admissible displacement field, minimizes the energy functional of a cracked solid. Therefore, the method directly reflects the idea of Griffith that a crack is formed such that the potential energy of the solid is minimized. In the wake of Bourdin's [9] work, many extensions of the approach to a variety of materials, such as ductile [10,11], visco-elastic [12], and heterogeneous materials [13] have already been made.

The original phase-field approach proposed by Bourdin lacks a nucleation threshold for the phase-field. This is especially relevant when the phase-field is considered irreversible. The reason is that the smeared crack energy functional cannot converge to that of the discrete case because any amount of strain will force the phase-field to accumulate which, in turn, brings the phase-field profile away from the Γ – convergent profiles discussed in Bourdin et al. [9]. Furthermore, in cases without a long initial crack (relative to the material's process zone size),

the global strength depends strongly on the regularization length. Both of these effects lead to a prediction of the mechanical response of a structure to be greatly dependent on the regularization length.

Attempts to reconcile these issues have been proposed by regarding the length scale as a material property or via modifications to the energy functional. The interpretation of the length scale as a material property [14] becomes problematic when the length scale is too large relative to the problem geometry, as the representation of the phase-field as a crack is lost. Modifications to the energy functional to establish a length scale independent strength (that is, a threshold for the accumulation of the phase-field) were first explored by Lorentz et al. [15] and later by Wu [16] and Geelen et al. [17]. These contributions consider quasi-brittle materials, such as concrete, where cohesive tractions exist for a considerable distance (which is referred to as the fracture process zone) behind the crack tip due to effects such as microcrack nucleation and coalescence. These considerations provide a more detailed abstraction of failure in brittle materials, which cannot be ignored at smaller length scales, compared to the idealization that there are no tractions behind the crack tip and that the stress at the crack tip is infinite. The implementation of the quasi-brittle phase-field models overwhelmingly involves the use of a strain energy history field [18] to replace the variational inequality (resulting from the principle of maximum dissipation) that governs the evolution of the phase-field with an equality. This approach leads to an undesirable widening of the phase-field profile, as is shown in subsequent sections, which leads to an overestimation of the amount of energy dissipated due to fracture. On the other hand, more rigorous methods, such as penalty [19], active set [20] and augmented Lagrangian methods [21], to solve the inequality problem have been proposed but have not been widely adopted, especially in implementations with commercial programs. This is likely due to the additional implementation and computational complexities associated with these approaches.

The phase-field modeling of ductile fracture is complicated by crack paths which are not necessarily (and frequently are not) equivalent to crack paths of brittle or quasi-brittle fracture. An intricate approach to capture many of the stress-state contingencies on material stability was developed by Li et al. [22] where stress triaxiality and Lode angle affect the initiation and propagation of a crack. However, this model does not include the fracture toughness as a material model parameter. Another novel ductile fracture model was proposed by Han et al. [23] where the elastic strain and plastic dissipation energies are degraded by separate phase fields. This model also considers the length scale parameters to be material properties. To the best of the authors' knowledge, the first ductile phase-field fracture model to consider a length scale independent local strength based on the approach of Lorentz et al. [15] was the model proposed by Hu et al. [24].

To circumvent the aforementioned issues, we propose an alternative coupling between the phase-field and mechanical fields. The proposed approach avoids a direct coupling of the elastic strain energy and phase-field. Instead, new internal variables are introduced which couple to the elastic strain energy and the phase-field where the phase-field controls the isotropic contraction of the failure surface associated with the newly introduced internal variables. Our proposed approach is just as simple to implement as the history field approach, provides an optimal phase-field profile, and is able to provide results which are objective with respect to the length scale. Further, it can represent quasi-brittle cracking behavior where a crack propagates with a tensile, opening character, and ductile cracking behavior where a crack propagates with a shearing, sliding character. The remainder of the paper is organized as follows. In Section 2, previous phase-field fracture models are briefly discussed, then, we present our formulation of the phase-field fracture model with infinite support of the phase-field. In Section 3, we present several numerical examples for one-dimensional (1D) and two-dimensional (2D) cases, along with experimental verifications of a quasi-brittle 3-point bending test and a ductile shear test, as well as a discussion of our results. In Section 4, we conclude the paper.

2. Phase-Field models of fracture

2.1. Phase-field regularizations of a discrete crack surface

For a solid domain Ω with a boundary S and a crack, Γ, the surface energy functional of the crack, Ψ^f, is defined as:

$$\Psi^f = \int_\Gamma G_c d\Gamma \tag{1}$$

where G_c is the critical energy release rate. The so-called AT-2 (Ambrosio – Tortorelli) [9] regularization approximates (1) as:

$$\Psi^f \approx \int_\Omega \psi^{AT2}(\phi)d\Omega = \int_\Omega G_c\left(\frac{\phi^2}{2L} + \frac{L}{2}|\nabla\phi|^2\right)d\Omega \tag{2}$$

where ϕ is the crack phase-field and L is the length scale parameter. In 1D setting, the Euler-Lagrange equation of (2) is given by:

$$-L^2\frac{d^2\phi}{dx^2} + \phi = 0 \tag{3}$$

which produces the solution:

$$\phi(x) = e^{-\frac{|x|}{L}} \tag{4}$$

where $\phi(0) = 1$ and $\lim_{x\to\pm\infty}\phi(x) = 0$. On the other hand, the so-called AT-1 [25] regularization approximates (1) as:

$$\Psi^f \approx \int_\Omega \psi^{AT1}(\phi)d\Omega = \int_\Omega \frac{3}{4}G_c\left(\frac{\phi}{L} + \frac{L}{4}|\nabla\phi|^2\right)d\Omega \tag{5}$$

In 1D, the Euler-Lagrange equation of (5) is given by:

$$-\frac{L^2}{2}\frac{d^2\phi}{dx^2} + 1 = 0 \tag{6}$$

which produces the solution:

$$\phi(x) = \begin{cases} 0, x < -L \\ \left(1 - \frac{|x|}{L}\right)^2, -L \leq x \leq L \\ 0, x > L \end{cases} \tag{7}$$

where $\phi(0) = 1$, $\phi(x > L) = 0$, and $\phi(x < -L) = 0$. The phase-field profile for the AT-1 model is thus a function with the closed support $[-L, L]$. This feature allows the model to admit a purely elastic domain (ϕ remains 0) prior to the development of fracture. In previous models, this feature has been exploited to enhance the phase-field fracture approach with a nucleation threshold for the phase-field. In all of the phase-field regularizations, the solution of ϕ is subject to the constraint that $\phi \in [0, 1]$.

2.2. Model A: Phase-field model of brittle fracture based on the AT-2 regularization

The earliest of the phase-field fracture models was proposed by Bourdin et al. [8] which considered the AT-2 regularization of the crack surface. Similar models based on the AT-2 model have been proposed by Miehe [26] as well. The mechanical fields, such as displacement, are coupled to the phase-field variable through a quadratic degradation function, $g_q(\phi)$. The energy density of this kind of model is given by:

$$\psi = \psi^e(\boldsymbol{\varepsilon}, \phi) + \psi^{AT2}(\phi) \tag{8}$$

here, we focus on a specification of the energy density which describes an elastically isotropic material and allows for the development of cracking to distinguish tensile stress states from compressive stress states through an additive split of the elastic strain energy into a degraded and undegraded component (ψ_0^e). Many forms of the energy density splitting

technique exist and have been reviewed in [27] which discussed the merits and drawbacks of several approaches. For simplicity, we focus on the following split technique to recover the Rankine, or maximum principal stress, yield criterion. ε is the engineering (small) strain and ψ^e is the elastic strain energy density which is given as:

$$\psi^e = \psi_0^e + \left[g_q(\phi) - 1\right]\overline{\psi}^e(\varepsilon) \tag{9}$$

$$g_q(\phi) = (1 - \phi)^2 \tag{10}$$

$$\psi_0^e = \frac{1}{2}KI_1(\varepsilon) + 2GJ_2(\varepsilon) \tag{11}$$

$$\overline{\psi}^e = \frac{1}{2(\lambda + 2\mu)} < \overline{\sigma}_1 >_+^2 \tag{12}$$

This strain energy density considers the maximum principal stress criterion for the fracture strength. K and G are the bulk and shear moduli of isotropic elasticity while I_1 and J_2 denote the first invariant and second deviatoric invariant respectively. λ and μ are the Lame parameters and $\overline{\sigma}_1$ is the undamaged first principal stress given by:

$$\overline{\sigma}_1 = (\lambda + 2\mu)\varepsilon_1 + \lambda\varepsilon_2 + \lambda\varepsilon_3 = (\lambda + 2\mu)\varepsilon : (e_1 \otimes e_1) + \lambda\varepsilon : (e_2 \otimes e_2) + \lambda\varepsilon$$
$$: (e_3 \otimes e_3) \tag{13}$$

where ε_i are the principal strains and e_i are the principal directions. Furthermore, $\langle x \rangle_+ = \frac{1}{2}(|x| + x)$ and $\langle x \rangle_- = \frac{1}{2}(|x| - x)$; these operators are used to prevent crack growth in compression. ε is defined under the small displacement assumption, which is considered for the remainder of this paper, as:

$$\varepsilon = \frac{1}{2}(\nabla^T u + \nabla u) \tag{14}$$

where u represents displacement. Considering the elastic strain energy (9), the stress is also defined as:

$$\sigma = \frac{\partial\psi^e}{\partial\varepsilon} \tag{15}$$

which is the definition of stress used throughout the remainder of this paper, although the specific form of the elastic strain energy will change. For the specific model considered here, the stress is given as:

$$\sigma = \frac{\partial\psi^e}{\partial\varepsilon} = \frac{\partial\psi_0^e}{\partial\varepsilon} + \left[g_q(\phi) - 1\right]\frac{\partial\overline{\psi}^e}{\partial\overline{\sigma}_1}\frac{\partial\overline{\sigma}_1}{\partial\varepsilon} = C$$
$$: \varepsilon + \left[g_q(\phi) - 1\right]H(\overline{\sigma}_1)\left[e_1 \otimes e_1 + \frac{\lambda}{2\mu + \lambda}(e_2 \otimes e_2 + e_3 \otimes e_3)\right] \tag{16}$$

where C is the isotropic elastic tensor and $H(x)$ is the Heaviside function. The equilibrium equations of the coupled displacement – phase-field problems are developed through thermodynamic and variational principles (discussed in Appendix A) and are given by the following strong form equations:

$$\nabla \bullet \sigma = 0 \tag{17}$$

$$\Phi^f = -g_q'(\phi)\overline{\psi}^e - G_c\left(\frac{\phi}{L} - L\nabla^2\phi\right) \leq 0, \dot{\phi} \geq 0, \dot{\phi}\Phi^f = 0 \tag{18}$$

Examination of (18) leads to the conclusion that any strain will cause ϕ to accumulate. As a matter of fact, the maximum critical local strength, σ_c, in 1D is given in [28]:

$$\sigma_c = \frac{9}{16}\sqrt{\frac{EG_c}{6L}} \tag{19}$$

where E is the elastic modulus. Equation (19) shows that as L is made smaller, the local strength of the material is predicted to increase. This is especially problematic for cases which involve the nucleation of cracks. Furthermore, when the development of ϕ is considered to be irreversible, the distribution of ϕ in space will not be the same as the solution given in (4), which limits the accuracy of the diffuse approximation technique in approximating the surface energy functional of a discrete crack. This is because any value of strain energy density greater than zero will cause the phase-field to accumulate.

The constraint of $0 \leq \phi \leq 1$ is automatically fulfilled in this model by the choice of the quadratic degradation function and the AT-2 regularization of the crack surface. However, the constraint $\dot{\phi} \geq 0$ requires an additional strategy. The most common approach to enforce this constraint is the so-called history field approach introduced by Miehe [26] which replaces $\overline{\psi}^e$ in (12) with the following:

$$\mathscr{H}_{n+1} = \max(\overline{\psi}_{n+1}^e, \mathscr{H}_n) \tag{20}$$

where n indicates the previous solution increment. Alternatives to this strategy include the penalty method [19], Lagrange multiplier method [29], or the augmented Lagrangian method [21]. The use of the history field approach greatly simplifies the finite element implementation of the model because it allows (15) to be written as an equality:

$$g_q'(\phi)\mathscr{H}_{n+1} + G_c\left(\frac{\phi}{L} - L\nabla^2\phi\right) = 0 \tag{21}$$

Remark. *In Bourdin's original model [8], a fully damaged portion of material is considered with $\phi = 0$ and the fully intact material is considered with $\phi = 1$. Most of the phase-field fracture literature considers the opposite. Therefore, in our presentation of the model, we re-write the equations so that $\phi = 0$ represents the fully intact material while $\phi = 1$ represents the fully damaged material. Furthermore, Bourdin's original model does not distinguish the effect of compressive and tensile stress states and the first principal stress as (12) does; instead in the original model the entirety of the elastic strain energy was multiplied by $g_q(\phi)$. We have included the split strain energy density function to recover the maximum principal stress criterion and to maintain consistency with the other models presented here.*

2.3. Model B: Phase-field model of quasi–brittle fracture

To the best of our knowledge, Lorentz et al. [15,30] was the first to develop a formulation that guarantees a length scale independent local strength. The model of Lorentz et al. [30] also considers the AT-1 regularization of the crack surface which is coupled to mechanical fields through a rational degradation function, $g_r(\phi)$. The free energy density of the solid is given by:

$$\psi = \psi^e(\varepsilon, \phi) + \psi^{AT1}(\phi) \tag{22}$$

here ψ^e, the elastic strain energy, is given as:

$$\psi^e = \psi_0^e + [g_r(\phi) - 1]\overline{\psi}^e(\varepsilon) \tag{23}$$

$$g_r(\phi) = \frac{(1 - \phi)^2}{(1 - \phi)^2 + m\phi(1 + \phi)} \tag{24}$$

$$m = \frac{3G_c}{4L\psi_c} \tag{25}$$

where ψ_c is the maximum elastic strain energy the material can sustain. Furthermore, to ensure the convexity of $g_r(\phi)$, m must be greater than 3. This restriction on m places an upper bound restriction on the choice of L in the form of $L \leq \frac{G_c}{4\psi_c}$, which may limit the applicability of the model to large domains.

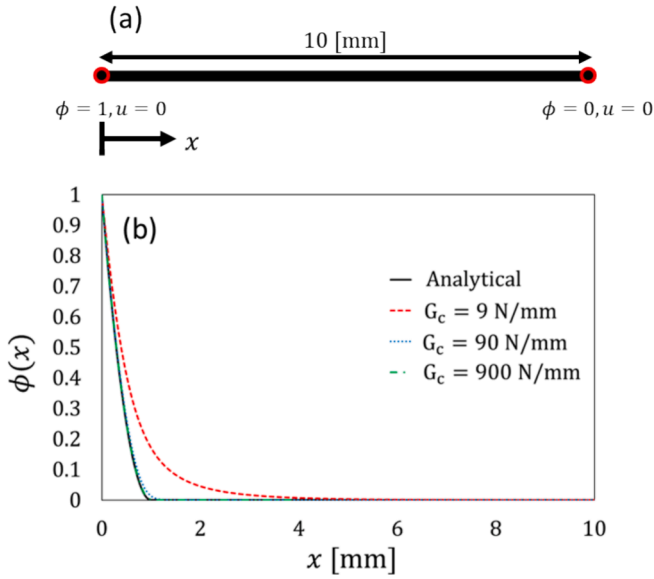Thermodynamic and variational arguments discussed in Appendix A provide the following strong form equations in Ω:

Fig. 1. (a) Domain and boundary conditions. (b) $\phi(x)$ with varying values of G_c to see the effect of an increasingly large value of m. For $G_c = 9, 90$, and 900 N/mm, $m = 3.14, 31.4$, and 314, respectively.

$$\nabla \bullet \boldsymbol{\sigma} = 0 \tag{26}$$

$$\Phi^f = -g_r'(\phi)\overline{\psi}^e - \frac{3}{4}G_c\left(\frac{1}{L} - \frac{L}{2}\nabla^2\phi\right) \leq 0, \dot{\phi} \geq 0, \dot{\phi}\Phi^f = 0 \tag{27}$$

And the weak form equations:

$$\int_\Omega \boldsymbol{\sigma} : \delta\boldsymbol{\varepsilon}(\boldsymbol{u})d\Omega - \int_S \boldsymbol{t} \bullet \delta\boldsymbol{u}dS = 0 \tag{28}$$

$$\int_\Omega -g_r'(\phi)\overline{\psi}^e\delta\phi - \frac{3}{4}G_c\left(\frac{1}{L}\delta\phi + \frac{L}{2}\nabla\phi \bullet \nabla\delta\phi\right)d\Omega \leq 0 \tag{29}$$

where δ indicates a variation.

A closer examination of (25) reveals how this model considers a local strength which is independent of the length scale. Prior to the development of any damage, ϕ is homogeneous and 0. Considering a 1D scenario and inserting $\phi(x) = 0$ into (27) yields:

$$g_r'(0)\overline{\psi}^e + \frac{3G_c}{4L} = -\frac{3G_c}{4L\psi_c}\overline{\psi}^e + \frac{3G_c}{4L} \leq 0 \tag{30}$$

when $\overline{\psi}^e < \psi_c$, the satisfaction of (27) as an equality would require ϕ to become negative, which violates the condition that $\dot{\phi} \geq 0$. Therefore, in the absence of pre-existing damage, when $\overline{\psi}^e < \psi_c$, ϕ must be 0. This feature gives the model a strain energy-based threshold on the accumulation of ϕ which is independent of the length scale, L. In other words, in order for ϕ to grow, $\overline{\psi}^e$ must be greater than ψ_c.

The Karush-Kuhn-Tucker constraints are typically dealt with by replacing $\overline{\psi}^e$ in (27) with the following, as has been done by [17,31–35]:

$$\psi^{Th} = \max(\overline{\psi}^e, \psi_c) \tag{31}$$

With the history field approach, we consider:

$$\mathscr{H}_{n+1} = \max(\psi^{Th}, \mathscr{H}_n) \tag{32}$$

so that the final form of the governing equations in strong form only involve equalities which read:

$$\nabla \bullet \boldsymbol{\sigma} = 0 \tag{33}$$

$$g_r'(\phi)\mathscr{H}_{n+1} + \frac{3}{4}G_c\left(\frac{1}{L} - \frac{L}{2}\nabla^2\phi\right) = 0 \tag{34}$$

However, this modification leads to a variational inconsistency and creates new issues. To see this, (34) is solved in 1D with the domain and boundary conditions as depicted in Fig. 1. In this example, L is 1 mm and ψ_c is 2.15 MPa.

In Fig. 1, the solution for $\phi(x)$ depends on the value of m. Furthermore, the solution only gets close to the analytically derived, Γ – convergent distribution of ϕ given in (7) when m is sufficiently large. The consequence is that for smaller values of m, the approximation to the surface energy given in (5) will be inaccurate. An alternative method to enforce the variational inequality can be developed using, for example, the penalty method [19]. Although this simple approach can reproduce the analytical profile in (7) for any value of m, the determination of the penalty stiffness requires problem dependent tuning. This is because a sufficiently high value of the penalty stiffness is required to adequately enforce the constraint, meanwhile, too high of a penalty stiffness makes convergence of the nonlinear solver challenging. This characteristic also applies to augmented Lagrangian approaches. Both approaches lead to implementational challenges and robustness issues. As a result of these numerical issues, the constraint enforcement strategy of (31 – 34) has been overwhelmingly used in the phase-field fracture literature and little attention has been given to the issue arising in Fig. 1.

2.4. Model C: Proposed phase-field model for quasi-brittle fracture

Before introducing the newly developed model, we recall the issues with the other approaches that have been discussed. In Model A, the lack of a nucleation threshold causes the local material strength to be dependent on the regularization length scale and the phase-field profile will differ from the optimal profile of Eq. (4). In Model B, the optimal phase-field profile of Eq. (7) cannot be reproduced with smaller values of the parameter m. To overcome these issues, we developed a model where the phase-field is not directly coupled to the momentum balance. Instead, an additional internal variable subject to loading and unloading conditions affects the material stiffness. Specifically, we consider the following energy density:

$$\psi(\boldsymbol{u}, \gamma, \phi) = \psi^e(\boldsymbol{\varepsilon}, \gamma) + \psi^\gamma(\gamma, \phi) + \psi^{AT2}(\phi) \tag{35}$$

where ψ^γ is a damage energy density and γ is a new variable which represents an equivalent strain normalized to a critical strain, as will be further developed. The elastic strain energy is given by:

$$\psi^e = \psi_0^e + \left[\frac{1}{\gamma + 1} - 1\right]\overline{\psi}^e(\boldsymbol{\varepsilon}) \tag{36}$$

And ψ^γ is given by:

$$\psi^\gamma = g_q(\phi)\psi_c\gamma \tag{37}$$

Thermodynamic and variational arguments discussed in Appendix B provide the following strong form equations in Ω:

$$\nabla \bullet \boldsymbol{\sigma} = 0 \tag{38}$$

$$\Phi^\gamma = \frac{1}{(\gamma + 1)^2}\overline{\psi}^e - g_q(\phi)\psi_c \leq 0, \dot{\gamma} \geq 0, \dot{\gamma}\Phi^\gamma = 0 \tag{39}$$

$$\Phi^f = -g_q'(\phi)\psi^c\gamma - G_c\left(\frac{\phi}{L} - L\nabla^2\phi\right) \leq 0, \dot{\phi} \geq 0, \dot{\phi}\Phi^f = 0 \tag{40}$$

And the weak form equations:

$$\int_\Omega \boldsymbol{\sigma} : \delta\boldsymbol{\varepsilon}(\boldsymbol{u})d\Omega - \int_S \boldsymbol{t} \bullet \delta\boldsymbol{u}dS = 0 \tag{41}$$

$$\int_\Omega \left(\frac{1}{(\gamma + 1)^2}\overline{\psi}^e - g_q(\phi)\psi_c\right)\delta\gamma d\Omega \leq 0 \tag{42}$$

$$\int_\Omega g_q'(\phi)\psi_c\gamma\delta\phi + G_c\left(\frac{\phi}{L}\delta\phi + L\nabla\phi \bullet \nabla\delta\phi\right)d\Omega \leq 0 \tag{43}$$

The calculation of γ in a time discrete setting is provided by a predictor–corrector scheme:

$$\gamma^{tr} = \frac{\sqrt{\overline{\psi^e}} - \sqrt{g_q(\phi)\psi_c}}{\sqrt{g_q(\phi)\psi_c}} \tag{44}$$

where γ^{tr} is explicitly calculated by solving (38) set equal to 0 for γ. Then,

$$\gamma_{n+1} = \max(\max(\gamma^{tr}, \gamma_n), 0) \tag{45}$$

where γ_{n+1} denotes the current value of γ and γ_n denotes its previous value. (44) and (45) imply that γ will only be non-zero when $\overline{\psi^e}$ exceeds ψ_c. This property naturally places a threshold on the accumulation of ϕ since the term $g_q'(\phi)\psi_c\gamma$ in (40) will be 0 when $\overline{\psi^e} < \psi_c$. Furthermore, irreversibility of the phase-field is automatically guaranteed through the irreversibility of γ. Additionally, no special treatment is required for the equilibrium equation of the phase-field since the AT-2 regularization was adopted which produces the profile of (4). With these properties, the inequality constraints in (40) are always fulfilled as long as the constraints on γ are fulfilled. Therefore, ϕ can be directly calculated from the following equality:

$$g_q'(\phi)\psi^c\gamma + G_c\left(\frac{\phi}{L} - L\nabla^2\phi\right) = 0 \tag{46}$$

To gain some intuition for the model, we consider the 1D scenario with the assumption of a monotonically increasing strain. Then, (39) simplifies to:

$$\Phi^\gamma = \frac{1}{(\gamma+1)^2}\left(\frac{1}{2}E\varepsilon^2\right) - g_q(\phi)\left(\frac{1}{2}E\varepsilon_c^2\right) \leq 0, \dot{\gamma} \geq 0, \dot{\gamma}\Phi^\gamma = 0 \tag{47}$$

where σ_c is the maximum stress attained by the material, E is Young's Modulus, and $\varepsilon_c = \frac{\sigma_c}{E}$. Because we have restricted ourselves to a monotonically increasing strain, γ can be written as:

$$\gamma = \begin{cases} \dfrac{\varepsilon - \sqrt{g_q(\phi)}\,\varepsilon_c}{\sqrt{g_q(\phi)}\,\varepsilon_c} = \dfrac{\varepsilon - (1-\phi)\varepsilon_c}{(1-\phi)\varepsilon_c}; \varepsilon > \varepsilon_c \\ 0; \varepsilon \leq \varepsilon_c \end{cases} \tag{48}$$

γ can now be interpreted as a strain normalized to a critical strain. The stress can then be written as:

$$\sigma = \left(\frac{1}{\gamma+1}\right)E\varepsilon = \begin{cases} (1-\phi)E\varepsilon_c; \varepsilon > \varepsilon_c \\ E\varepsilon; \varepsilon \leq \varepsilon_c \end{cases} \tag{49}$$

Therefore, when the phase-field is neglected, the model features a stress–strain relation that is linear until the strain reaches ε_c and then, the stress plateaus at σ_c. With the phase-field, the stress decreases from σ_c by a factor of $g_q(\phi)$ until reaching 0 when $\phi = 1$. The homogeneous stress–strain response for this model can be calculated by setting $\nabla^2\phi$ to 0 in (45). Then, we have:

$$(\phi - 1)E\varepsilon_c^2\gamma + G_c\frac{\phi}{L} = 0 \tag{50}$$

Inserting the non-zero subset of γ from (48) into (50) yields a relationship for ϕ:

$$\phi = \begin{cases} 1; \varepsilon \geq \dfrac{G_c}{LE\varepsilon_c} \\ \dfrac{E\varepsilon_c^2 - E\varepsilon_c\varepsilon}{E\varepsilon_c^2 - \dfrac{G_c}{L}}; \varepsilon_c < \varepsilon < \dfrac{G_c}{LE\varepsilon_c} \\ 0; \varepsilon \leq \varepsilon_c \end{cases} \tag{51}$$

(51) can then be inserted back into (49) to produce the homogeneous, 1D stress–strain response:

$$\sigma = \begin{cases} 0; \varepsilon \geq \dfrac{G_c}{LE\varepsilon_c} \\ E\varepsilon_c\dfrac{\dfrac{G_c}{L} - E\varepsilon_c\varepsilon}{\dfrac{G_c}{L} - E\varepsilon_c^2}; \varepsilon_c < \varepsilon < \dfrac{G_c}{LE\varepsilon_c} \\ E\varepsilon_c\varepsilon; \varepsilon \leq \varepsilon_c \end{cases} \tag{52}$$

Which corresponds to a situation of linear softening.

2.5. Model D: Phase-field model of ductile fracture

Having established the importance of including a threshold for damage, attention is given to the phase-field models of ductile fracture which are based on the model of Lorentz et al. [30]. To the best of our knowledge, Hu et al. [24] was the first to consider ductile fracture with a rational degradation function and the AT1 crack energy density. The free energy density of the elastic–plastic-fracturing solid with a rational degradation function and AT1 crack energy density is given by:

$$\psi = \psi^e(\varepsilon, \varepsilon^p, \phi) + \psi^p(\alpha, \phi) + \psi^{AT1}(\phi) \tag{53}$$

where α is the equivalent plastic strain, and ψ^p is the plastic energy density which is given as:

$$\psi^p = g_r(\phi)\overline{\psi^p} \tag{54}$$

$$\overline{\psi^p} = \int_0^\alpha \sigma_y(\alpha)d\alpha \tag{55}$$

here, $\sigma_y(\overline{e}^p)$ is the yield strength. The elastic strain energy is given by:

$$\psi^e = \psi_0^e + [g_r(\phi) - 1]\overline{\psi^e}(\varepsilon) \tag{56}$$

$$\varepsilon^e = \varepsilon - \varepsilon^p \tag{57}$$

$$\varepsilon^p = \alpha\frac{\partial \Phi^p(\sigma)}{\partial \sigma} \tag{58}$$

where ε^p is the plastic strain tensor, and $\Phi^p(\sigma)$ is the equivalent stress for plastic deformation which is given as the von Mises yield surface:

$$\Phi^p = \sqrt{3J_2(\sigma)} - g_r(\phi)\sigma_y(\alpha) \tag{59}$$

where J_2 is the second invariant of the deviatoric stress.

Thermodynamic and variational arguments discussed in Appendix A provide the following strong form equations in Ω:

$$\nabla \bullet \sigma = 0 \tag{60}$$

$$\Phi^p = \sqrt{3J_2(\sigma)} - g_r(\phi)\sigma_y(\alpha) \leq 0, \dot{\alpha} \geq 0, \dot{\alpha}\Phi^p = 0 \tag{61}$$

$$\Phi^f = -g_r'(\phi)(\overline{\psi^e} + \overline{\psi^p}) - \frac{3}{4}G_c\left(\frac{1}{L} - \frac{L}{2}\nabla^2\phi\right) \leq 0, \dot{\phi} \geq 0, \dot{\phi}\Phi^f = 0 \tag{62}$$

And the weak form equations:

$$\int_\Omega \sigma : \delta\varepsilon(u)d\Omega - \int_S t \bullet \delta u dS = 0 \tag{63}$$

$$\int_\Omega \left(\sqrt{3J_2(\sigma)} - g_r(\phi)\sigma_y(\alpha)\right)\delta\alpha d\Omega \leq 0 \tag{64}$$

$$\int_\Omega g_r'(\phi)(\overline{\psi^e} + \overline{\psi^p})\delta\phi + \frac{3}{4}G_c\left(\frac{1}{L}\delta\phi + \frac{L}{2}\nabla\phi \bullet \nabla\delta\phi\right)d\Omega \leq 0 \tag{65}$$

Taking a similar constraint enforcement strategy to the one given in (31–32), the history field approach is used to re-write (65) as an

equality:

$$g_r'(\phi)(\mathscr{H}_{n+1}) + \frac{3}{4}G_c\left(\frac{1}{L} - \frac{L}{2}\nabla^2\phi\right) = 0 \tag{66}$$

$$\mathscr{H}_{n+1} = \max(\psi^{Th}, \mathscr{H}_n) \tag{67}$$

$$\psi^{Th} = \max(\overline{\psi}^e + \overline{\psi}^p, \psi_c) \tag{68}$$

This produces the same problem with the phase-field profile that was discussed in sub-section 2.3, where the computed profile can only recover the quadratic profile from (7) when $m \to \infty$. Meanwhile, the inequality constrained problem of (64) can be solved using a return mapping scheme as discussed in [36].

2.6. Model E: Proposed phase-field model of ductile fracture

To model fractures which have a ductile, sliding character, a similar approach to the quasi-brittle case is taken. The free energy density is taken as:

$$\psi = \psi^e(\boldsymbol{\varepsilon}, \boldsymbol{\varepsilon}^p, \boldsymbol{\varepsilon}^s) + \psi^p(\alpha) + \psi^s(s, \phi) + \psi^{AT2}(\phi) \tag{69}$$

here, s is an equivalent inelastic strain that represents localized shear or sliding, $\boldsymbol{\varepsilon}^s$ is the inelastic strain tensor associated with this localized sliding and ψ^s will be referred to as the sliding energy density. Furthermore, $\boldsymbol{\varepsilon}^s$ is constructed as a deviatoric tensor and is only non-zero during softening to elicit a sliding type of response. The elastic strain energy is given as:

$$\psi^e = \frac{1}{2}KI_1^2(\boldsymbol{\varepsilon}^e) + 2GJ_2(\boldsymbol{\varepsilon}^e) \tag{70}$$

$$\boldsymbol{\varepsilon}^e = \boldsymbol{\varepsilon} - \boldsymbol{\varepsilon}^p - \boldsymbol{\varepsilon}^s \tag{71}$$

The plastic energy density, ψ^p, is given as:

$$\psi^p = \int_0^\alpha \sigma_y(\alpha)d\alpha \tag{72}$$

The sliding energy density, ψ^s, is given as:

$$\psi^s = g_q(\phi)\tau_c s \tag{73}$$

where τ_c is a critical stress to initiate a sliding type of fracture. Thermodynamic and variational considerations discussed in Appendix C provide the following strong form equations in Ω:

$$\nabla \bullet \boldsymbol{\sigma} = 0 \tag{74}$$

$$\Phi^p = \sqrt{3J_2(\boldsymbol{\sigma})} - \sigma_y(\alpha) \leq 0, \; \dot{\alpha} \geq 0, \dot{\alpha}\Phi^p = 0 \tag{75}$$

$$\Phi^s = \sqrt{3J_2(\boldsymbol{\sigma})} - g_q(\phi)\tau_c \leq 0, \; \dot{s} \geq 0, \dot{s}\Phi^s = 0 \tag{76}$$

$$\Phi^f = -g_q'(\phi)\tau_c s - G_c\left(\frac{\phi}{L} - L\nabla^2\phi\right) \leq 0, \; \dot{\phi} \geq 0, \dot{\phi}\Phi^f = 0 \tag{77}$$

And the weak form equations:

$$\int_\Omega \boldsymbol{\sigma}:\delta\boldsymbol{\varepsilon}(\boldsymbol{u})d\Omega - \int_S \boldsymbol{t}\bullet\delta\boldsymbol{u}dS = 0 \tag{78}$$

$$\int_\Omega \left(\sqrt{3J_2(\boldsymbol{\sigma})} - \sigma_y(\alpha)\right)\delta\alpha d\Omega \leq 0 \tag{79}$$

$$\int_\Omega \left(\sqrt{3J_2(\boldsymbol{\sigma})} - g_q(\phi)\tau_c\right)\delta s d\Omega \leq 0 \tag{80}$$

$$\int_\Omega g_q'(\phi)\tau_c s\delta\phi + G_c\left(\frac{\phi}{L}\delta\phi + L\nabla\phi\bullet\nabla\delta\phi\right)d\Omega \leq 0 \tag{81}$$

The inequality constrained problems of (79) and (80) are solved

using the return mapping procedure found in [36]. Similar to the case of Model C, the inequality constraints in (81) are always fulfilled as long as the constraints on s are fulfilled. Therefore, (81) can be re-written as an equality:

$$g_q'(\phi)\tau_c\overline{\varepsilon}^s + G_c\left(\frac{\phi}{L} - L\nabla^2\phi\right) = 0 \tag{82}$$

Furthermore, with the omission of ψ^p from the energy density (69), material behavior similar to the one in Fei et al. [34,35],which was developed for sliding failures in geomaterials, can be recovered.

To gain some insight, we will consider a 1D case with the omission of ψ^p with a monotonically increasing strain. Furthermore, we will focus on the case of $\varepsilon > \left(\frac{\tau_c}{E}\right) = \varepsilon_c$. (74) simplifies to:

$$E(\varepsilon - s) - g_q(\phi)\tau_c = 0 \tag{83}$$

And so s can be written as:

$$s = \varepsilon - (1 - \phi)^2 \varepsilon_c$$

For the case of the homogeneous response, (82) can be written as:

$$2(\phi - 1)\tau_c s + \frac{G_c\phi}{L} = 0 \tag{84}$$

$$2(\phi - 1)\tau_c \left[\varepsilon - (1 - \phi)^2\varepsilon_c\right] + \frac{G_c\phi}{L} = 0$$

Which can be solved for ϕ by the cubic formula:

$$\phi = 1 + \left[q + \left(q^2 + (r - 1)^3\right)^{\frac{1}{2}}\right]^{\frac{1}{3}} + \left[q - \left(q^2 + (r - 1)^3\right)^{\frac{1}{2}}\right]^{\frac{1}{3}} \tag{85a}$$

$$q = 1 + \frac{1}{6}\left(\frac{6\varepsilon}{\varepsilon_c} - \frac{3G_c}{2L\tau_c\varepsilon_c} - 12\right) \tag{85b}$$

$$r = \frac{1}{3}\left(\frac{G_c}{2L\tau_c\varepsilon_c} - \frac{\varepsilon}{\varepsilon_c} + 3\right) \tag{85c}$$

Then, σ for the softening branch of the stress–strain curve can be written as:

$$\sigma = \left(\left[q + \left(q^2 + (r - 1)^3\right)^{\frac{1}{2}}\right]^{\frac{1}{3}} + \left[q - \left(q^2 + (r - 1)^3\right)^{\frac{1}{2}}\right]^{\frac{1}{3}}\right)^2 \tau_c \tag{86}$$

Remark. *Although the von Mises criterion is adopted for both yield surfaces, this choice is made only for simplicity in the stress integration procedure. Furthermore, Φ^p and Φ^s do not need to be the same; for example, the Hill-48 criterion [37] could be chosen for Φ^p while the Mohr-Coulomb criterion [38] could be chosen for Φ^s. Ultimately, the choice of these should be motivated by the specific material in question.*

2.7. Software implementation and solution scheme

The models B, C, D and E are discretized and solved with the finite element method through the COMSOL Multiphysics software. In all of the implemented models, both the displacement and phase-field weak form equations (26, 27, 41, 43, 63, 65, 78, 81) are discretized with linear Lagrange elements by the Galerkin method. Specifically, the mechanical sub-problem is implemented via the "Solid Mechanics Module" while the phase-field sub-problem is implemented via the "Weak Form PDE Module".

In some problems, an indirect displacement control technique was used to resolve the snap back in the force–displacement response. In order to apply the indirect displacement control, two nodes opposite to the crack face are chosen so that the difference in their displacement values ($\boldsymbol{u}_a$ and $\boldsymbol{u}_b$) is the crack opening displacement (**COD**). A constraint on the crack opening displacement is introduced as:

Table 1
Material properties for quasi-brittle case.

Property	Value
Young's Modulus, E	210 GPa
Fracture Strength, σ_f	360 MPa
Critical Energy Release Rate, G_c	2 N/mm

$$g(\boldsymbol{u}) = \boldsymbol{u}_a - \boldsymbol{u}_b - \mathbf{COD} = 0 \tag{87}$$

Meanwhile, an unknown load, $\boldsymbol{P}$ is applied to an edge of the domain, S. The equilibrium equation for $\boldsymbol{u}$ is:

$$\int_\Omega \frac{\delta\psi}{\delta\boldsymbol{u}}(\boldsymbol{u}, \cdots)\delta\boldsymbol{u}d\Omega - \int_S \boldsymbol{P} \bullet \delta\boldsymbol{u}dS = 0 \tag{88}$$

$\boldsymbol{P}$ can then be determined by solving (87) in conjunction with (88). More sophisticated path following constraints have been developed in [39] and [40] where the global rate of energy dissipation is controlled and used as a path following constraint. The approach taken here is different from these approaches in that we are only setting a constraint on a set of nodes on opposite sides of a crack face instead of a global constraint on the entire volume.

Further, the staggered solution scheme developed in [26] is used in all examples for its robustness. In the implemented staggered scheme, the problems are solved sequentially in the order of the equilibrium equation for ϕ and then the equilibrium equation $\boldsymbol{u}$. The staggered solver is given 10 iterations in each load increment. Furthermore, the solution of the nonlinear equilibrium equations for ϕ and the displacements were achieved through the standard Newton – Raphson method with a maximum of 20 iterations. If the solver does not converge after taking this many increments, the load increment is cut in half and re-solved.

3. Results and discussion

3.1. Homogeneous stress strain response

To demonstrate the stress–strain relations of the proposed phase-field fracture models (Models C and E), a case of homogeneous strain is considered. The model parameters for the quasi-brittle case are presented in Table 1. For the quasi-brittle case (Model C), the strain energy threshold, ψ_c, is set so that 1D fracture strength, σ_f, is 360 MPa by the relation:

$$\psi_c = \frac{\sigma_f^2}{2(2\mu + \lambda)} \tag{89}$$

Furthermore, for the ductile case, a linear strain hardening behavior is adopted, and the yield stress is given by:

$$\sigma_y(\alpha) = \sigma_{y0} + H_m\alpha \tag{90}$$

where σ_{y0} is the initial yield stress and H_m is the linear hardening modulus.

The stress–strain relations and unloading behaviors corresponding to these material parameters are plotted in Fig. 2.

The stress strain relations and unloading behaviors for Model B (the quasi-brittle model proposed by Geelen et al. [17]) and Model D (the ductile model proposed by Hu et al. [24]) are also shown in Fig. 3. The material properties for the quasi-brittle models are the same. For the ductile model, ψ_c is set so that the maximum stress matches τ_c by the following relation:

$$\psi_c = \frac{(\tau_c - \sigma_{y0})^2 + 2\sigma_{y0}(\tau_c - \sigma_{y0})}{2H_m} + \frac{\tau_c^2}{2E} \tag{91}$$

The proposed quasi-brittle stress–strain relation exhibits a linear softening behavior while Model B produces an exponential softening behavior. For both of the models, the unloading behavior is the same. On the other hand, for the ductile scenario, the proposed model does not reduce the elastic modulus during the damaging phase and inelastic
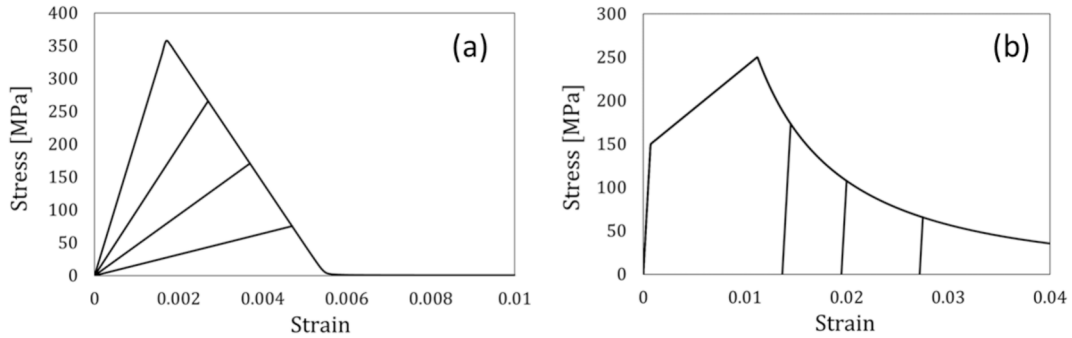

Fig. 2. Homogeneous stress strain curves produced by the proposed (a) quasi-brittle model (Model C) and (b) ductile model (Model E).
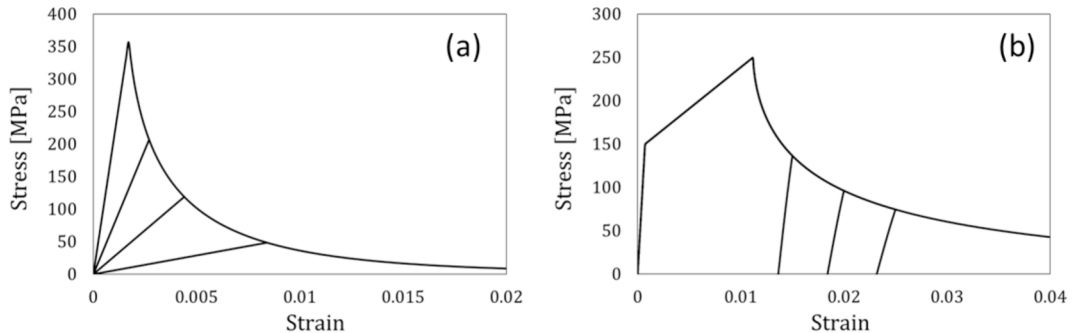

Fig. 3. Homogeneous stress strain curves produced by (a) Model B and (b) Model D.
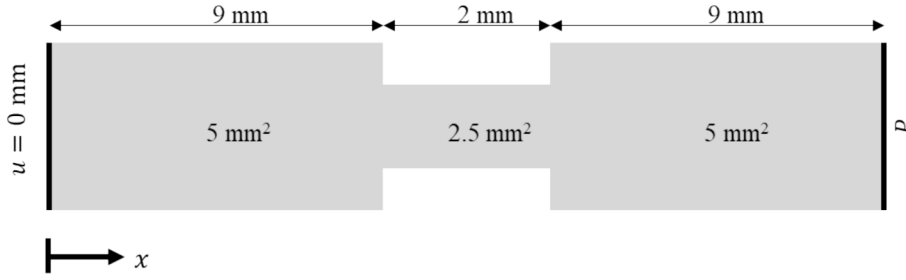
Fig. 4. Schematic and boundary conditions of 1D examples.

Table 2
Material properties for ductile case.

Property	Value
Young's Modulus,E	210 GPa
Plastic Yield Stress,σ_{y0}	150 MPa
Linear Hardening Modulus,H_m	10 GPa
Critical Stress,τ_c	250 MPa
Critical Energy Release Rate,G_c	9 N/mm

strain accumulates. Meanwhile, Model D produces a behavior of simultaneously reduced elastic modulus and inelastic strain accumulation.

3.2. 1D examples

A series of 1D examples are presented to illustrate the differences between the proposed phase-field fracture models (models C and E) and models B and D. 1D problems consist of a bar with a reduced cross section in the center to promote crack nucleation in the center of the bar. A schematic of the bar is shown in Fig. 4. The material properties from Table 1 and Table 2 are considered for the quasi-brittle and ductile scenarios, respectively.

The bar is meshed with a uniform element size of 0.0125 mm. In all of these cases, an indirect displacement control technique is used to trace the equilibrium path of scenarios involving snap-back. Specifically, P was computed such that the opening displacement increased linearly with the number of loading increments. It should be noted that the difference in $u(x = 10.0125\text{mm})$ and $u(x = 10\text{mm})$ is considered to measure the opening displacement.

First, the two quasi-brittle models are demonstrated across a variety of regularization lengths. The resulting stress-displacement responses are shown in Fig. 5.

Although Model B shows little sensitivity to the choice of the regularization length, there are slight differences between the curves, while the curves obtained by the proposed model (Model C) are virtually indistinguishable from each other. The phase-field profiles shown on Fig. 6 provide some insight to this difference.

The phase-field profile produced by Model B is noticeably thicker than the optimal, Γ- convergent profile of Equation (7). This is rooted in the same issue discussed in Section 2.3. This introduces error to the approximation of the crack surface energy which results in length scale sensitivity in the softening regime of the stress-displacement response. Next, the ductile scenario is considered, and the stress-displacement responses are shown in Fig. 7.

Once again, the stress-displacement responses of the proposed model
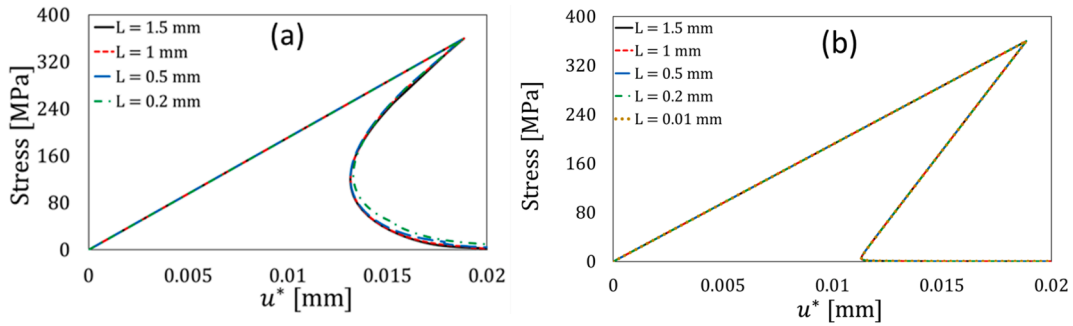

Fig. 5. Stress-displacement response of the quasi-brittle 1D tests: (a) Model B and (b) Model C (our proposed phase-field model for quasi-brittle fracture).
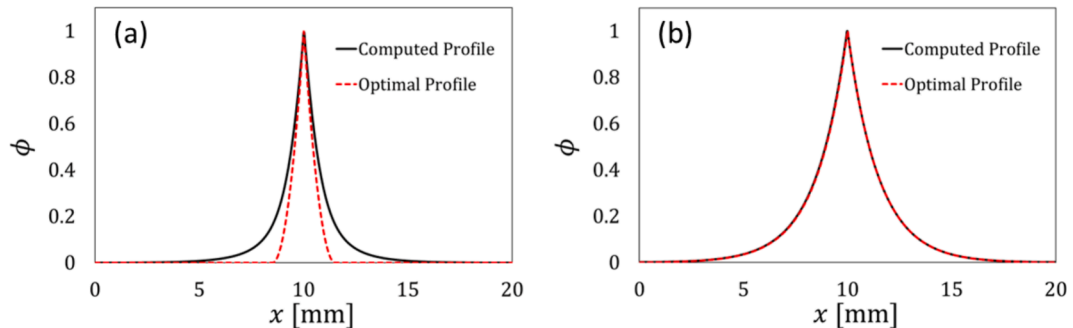

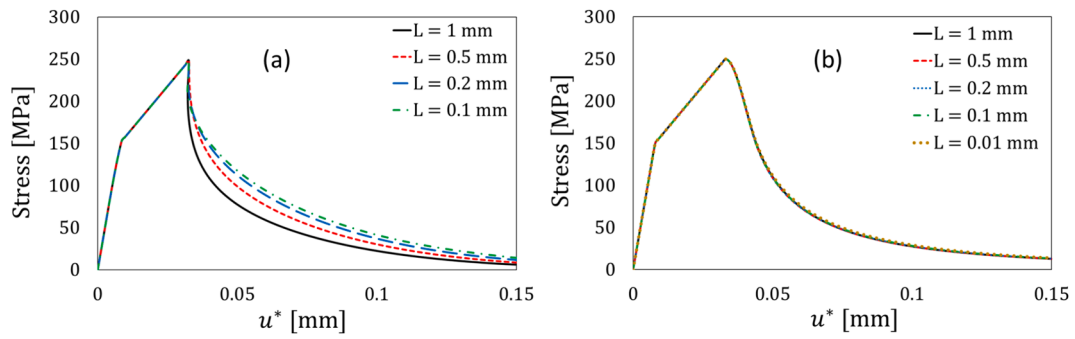**Fig. 6.** Phase-field profiles. (a) Model B for $L = 1.5$mm. (b) Model C for $L = 1.5$mm.

Fig. 7. Stress-displacement response of the ductile 1D tests: (a) Model D proposed by Hu et al. [24] (b) Model E (our proposed model).
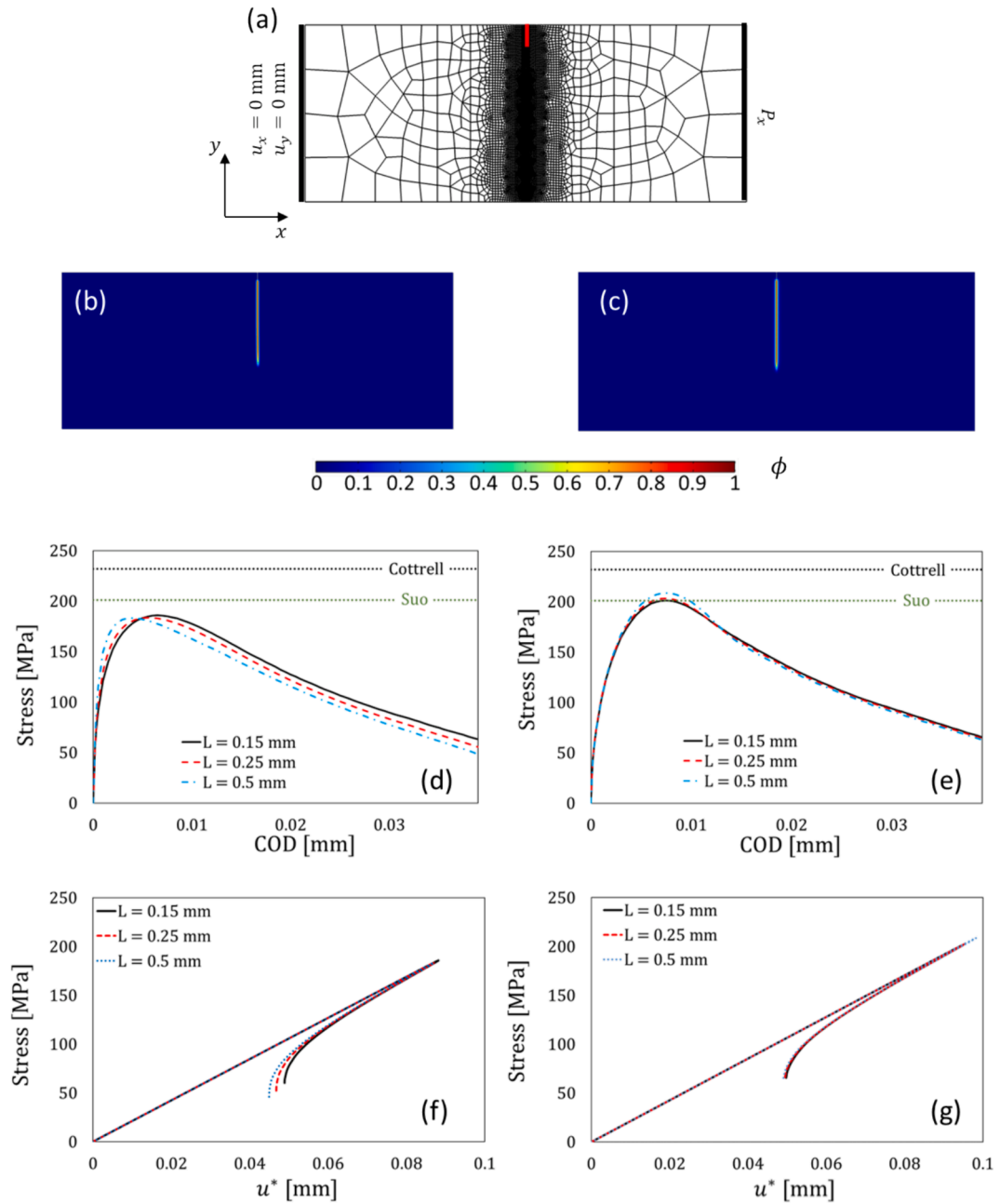

Fig. 8. (a) Mesh and Boundary Conditions. (b) Phase-field profile computed with model B taking $L = 1$ mm. (c) Phase-field profile computed with model C taking $L = 1$ mm. (d) Stress-Crack Opening Displacement predicted by model B. (e) Stress-Crack Opening Displacement predicted by model B. Mechanical response predicted by model C. (f) Stress-Displacement response predicted by model B. (g) Stress-Displacement response predicted by model C.
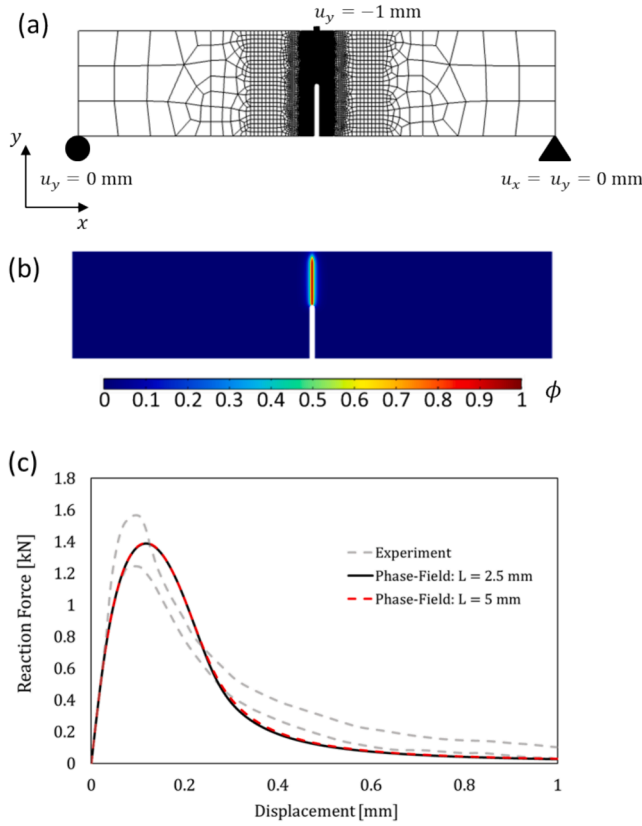
Fig. 9. (a) Mesh and Boundary Conditions. (b) Phase-field profile computed with model C taking $L = 2.5$ mm. (c) Mechanical response predicted by model C.

(Model E) across several regularization lengths are indistinguishable. Meanwhile, Model D displays a greater sensitivity to the regularization length. The sensitivity here is rooted in the same issue that affected Model B where the AT-1 crack profile cannot be reproduced when m is too small. Furthermore, it can be seen that as m is increased by decreasing the regularization length, the stress-displacement curves begin to converge.

3.3. 2D quasi-brittle examples

Having established the effectiveness of the proposed quasi-brittle model in 1D, attention is given to the performance in 2D and its capability to reproduce the mechanical response of a concrete beam. First, we compare the effect of the regularization length on the proposed model (Model C) and that of Model B. To this end, a plane stress tensile test on a rectangular domain with dimensions of 200 by 100 mm with a 4 mm edge crack with the same material parameters considered in the quasi-brittle 1D examples, along with a Poisson ratio of 0.3 is considered. Once again, an indirect displacement control technique is used where the load is computed such that a constraint on the crack opening displacement is satisfied. The mesh and boundary conditions, as well as the phase-field profiles and load–displacement curves are shown in Fig. 8. The strength predictions are also compared to the numerical predictions from a cohesive zone model with linear softening considered by Suo [41] as well as the analytical predictions of strength resulting from the Dugdale [42] cohesive zone model considered by Cottrell [43]. The strength (σ_c) predicted by the Cotrell model (for an infinite plate) is given as:

$$\sigma_c = \frac{2}{\pi}\sigma_f \arccos\left[exp\left(-\frac{\pi E G_c}{8\sigma_f^2 a}\right)\right] \tag{92}$$

Table 3
Material properties for quasi-brittle beam.

Property	Value
Young's Modulus, E	20 GPa
Poisson Ratio, ν	0.2
Fracture Strength, σ_f	2 MPa
Critical Energy Release Rate, G_c	0.08 N/mm

where σ_f is the cohesive strength and a is the half crack length.

The proposed model shows virtually no effect of the regularization length on the load–displacement response and converges to the same strength prediction resulting from Suo's [41] cohesive zone modeling. Meanwhile, Model B shows a slight difference in the predicted strength and failure displacement. Additionally, the two models predict slightly different strengths. This effect can be attributed to the difference in softening responses at the level of a volume element shown in Figs. 2 and 3.

Next, attention is given to the capability of the proposed model to capture the mechanical response of a concrete beam under bending. This experiment was presented by Rots [44] and consists of a 450 mm by 100 mm concrete specimen with an edge notch which is 50 mm deep and 5 mm wide. Furthermore, a state of plane stress is assumed in the simulations. The mesh and boundary conditions, as well as the phase-field profiles and load–displacement curves are shown in Fig. 9. The material properties used for this example are presented in Table 3. Although the elastic properties are the same, the damage properties had to be calibrated and differ from those used by Rots [44] because an exponential softening relationship was considered there to calibrate the damage properties.

Once again, the load displacement curves are indistinguishable across the two values of the regularization length. Furthermore, the proposed model is able to predict the strength of the concrete specimen. Although the softening portion of the load–displacement curve falls slightly outside of the experimental range, it is likely that more calibration or slight modifications to the model could bring the softening prediction closer to the experimental range (specifically regarding the shape of the softening regime in the local stress–strain response).

3.4. 2D ductile fracture examples

Next, we consider the ductile case in 2D. First, the direct shear of a notched plate is considered, and the proposed ductile fracture modeling approach (Model E) is compared to the one proposed by Hu et al. [24] (Model D). Specifically, the cross section considered in this example measures 50 mm by 15 mm with two symmetric edge notches which are 5 mm deep and 2.5 mm wide. A state of plane strain is assumed. Furthermore, the material properties are taken to be identical to those in the 1D ductile examples with a Poisson ratio of 0.3. The mesh and boundary conditions, as well as the phase-field profiles and load–displacement curves are shown in Fig. 10.

Similar to the quasi-brittle case, the proposed model shows no sensitivity to the choice of regularization length. On the other hand, the model, proposed by Hu et al. [24], which combines a rational degradation function and AT-1 crack regularization produces a regularization length dependent load–displacement response.

Next, a case of tension is considered with the same material properties. A plane strain strip which has dimensions of 10 mm by 50 mm with a 1 mm radius notch located in the lower right corner of the strip is considered. The mesh and boundary conditions, as well as the phase-field profiles and load–displacement curves are shown in Fig. 11.

The load–displacement curve produced by the proposed ductile fracture model is insensitive to the choice of regularization length. Furthermore, because the plane of maximum shear stress is 45 degrees from the loading axis, we expect a ductile fracture to develop with a slanted orientation close to the plane of maximum shear. The proposed
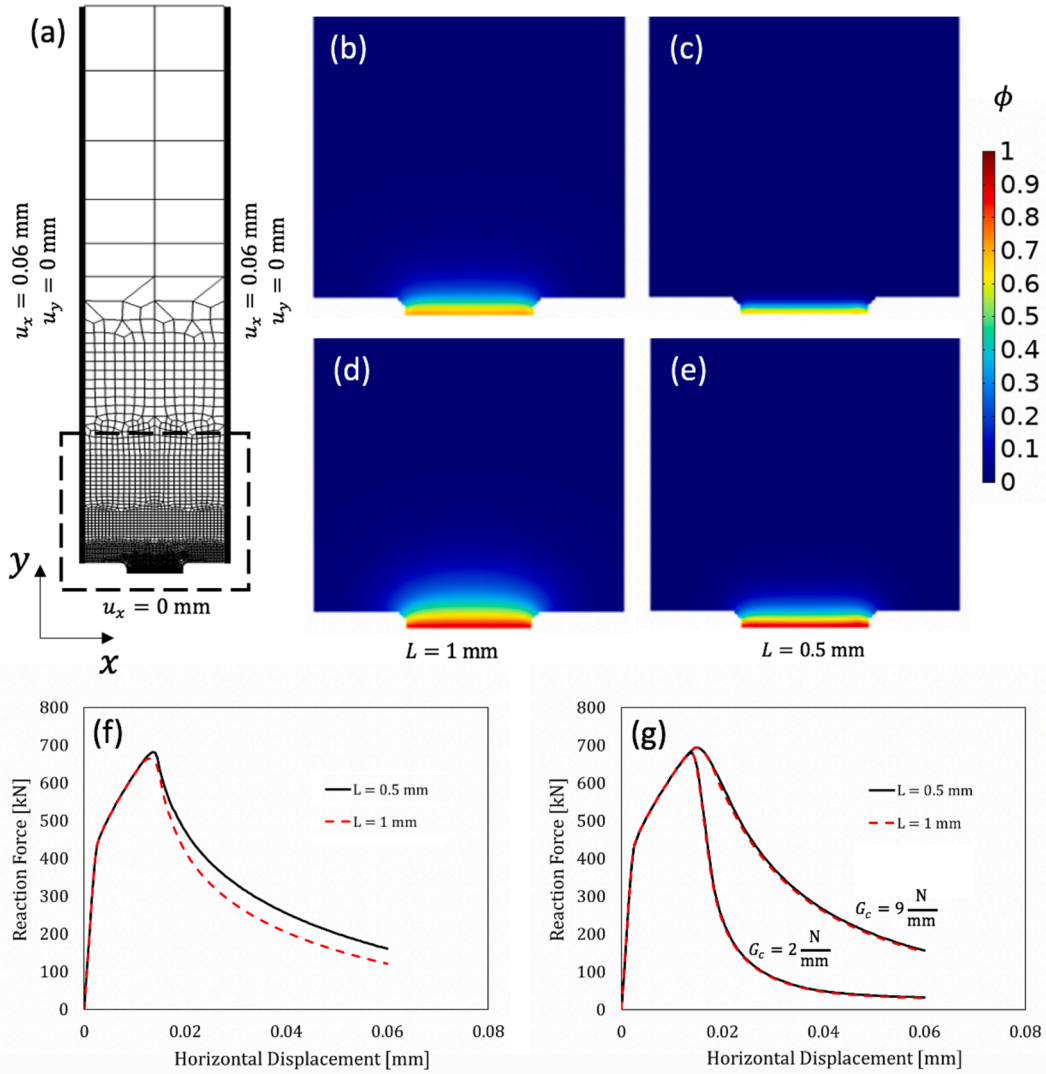
Fig. 10. (a) Mesh and Boundary Conditions. (b) Phase-field profile computed with model D taking $L = 1$ mm. (c) Phase-field profile computed with model D taking $L = 0.5$ mm. (d) Phase field profile computed with model E taking $L = 1$ mm. (e) Phase-field profile computed with model E taking $L = 0.5$ mm. (f) Mechanical response predicted by model D. (g) Mechanical response predicted by model E.

model is capable of predicting this phenomenon.

Finally, we consider the shear fracture experiment of a steel sheet conducted by Khameneh et al. [45]. A state of plane stress is assumed and the mesh and boundary conditions, as well as the phase-field profile and stress-displacement curve are shown in Fig. 12. A piecewise linear hardening model is adopted for the plastic hardening response. The material parameters used are presented in Table 4 and Table 5.

The proposed approach to model ductile fracture is capable of predicting the experimentally observed stress-displacement response. As expected, the crack nucleates and propagates almost parallel to the loading axis because the plane of maximum shear stress exists approximately parallel to the loading direction for this specimen's geometry. Furthermore, unlike the ductile fracture models proposed by Ambati et al. [46] and Mueller et al. [47], which do not feature a damage threshold, the plastic properties of the material can be calibrated independent of the phase-field model. This feature of the proposed model makes the model calibration with a real material behavior significantly easier.

4. Conclusion

A critical analysis of the existing phase-field approaches for quasi-

brittle and ductile fracture was presented, and two alternative phase-field approaches were developed and advanced in this contribution. The developed approaches do not rely on the phase-field profile to set a threshold for the nucleation of the phase-field. Instead, additional dissipation terms are introduced to the energy functional which allow for the definition of a stress or strain-based threshold in conjunction with the use of the AT-2 regularization (Ambrosio – Tortorelli) [9]. This approach eliminates the need for the enforcement of the irreversibility constraint on ϕ or the $\phi \geq 0$ constraint in the equilibrium equation for the phase-field by means of the history field, penalty, or Lagrange multiplier methods. Instead, the proposed modelling approach takes a simpler approach which enforces irreversibility constraints on two additional internal variables which are updated by explicit closed form evolution equations. This, in turn, leads to a solution process where the irreversibility constraint on ϕ is fulfilled by solving a single equality. Furthermore, the approach does not restrict the choice of regularization length scale parameter, as is necessitated by previous models [13–15], which makes the proposed method attractive for use in larger scale scenarios. Additionally, the automatic satisfaction of the constraints on the phase-field makes the proposed method simple for implementation in commercial finite element programs.

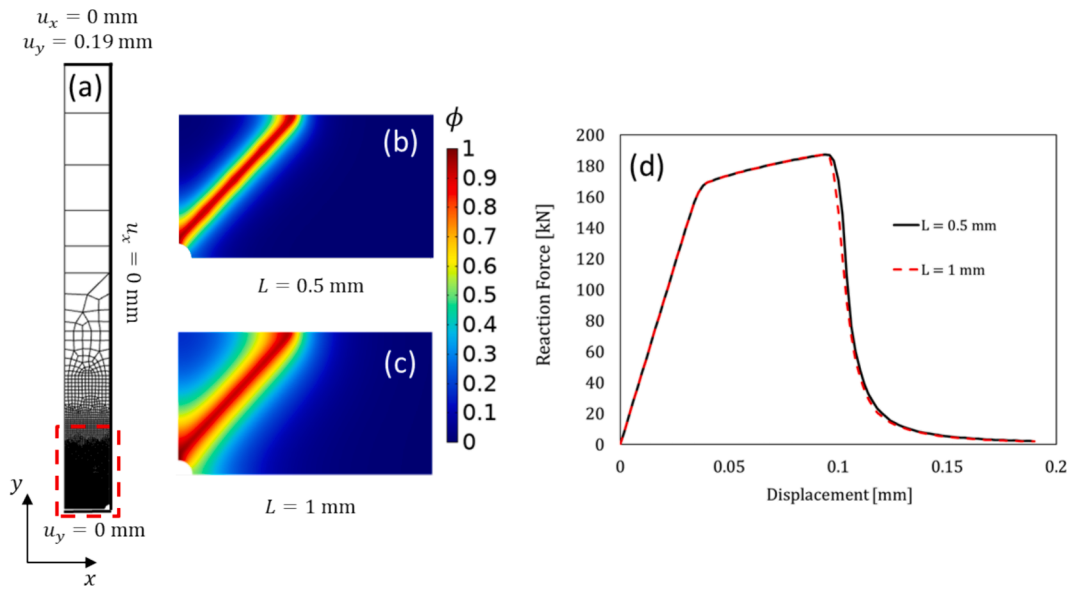The proposed approach was able to reproduce experimental results

Fig. 11. (a) Mesh and Boundary Conditions. (b) Phase-field profile computed with model E taking $L = 0.5$ mm. (c) Phase-field profile computed with model E taking $L = 1$ mm. (d) Mechanical response predicted by model E.
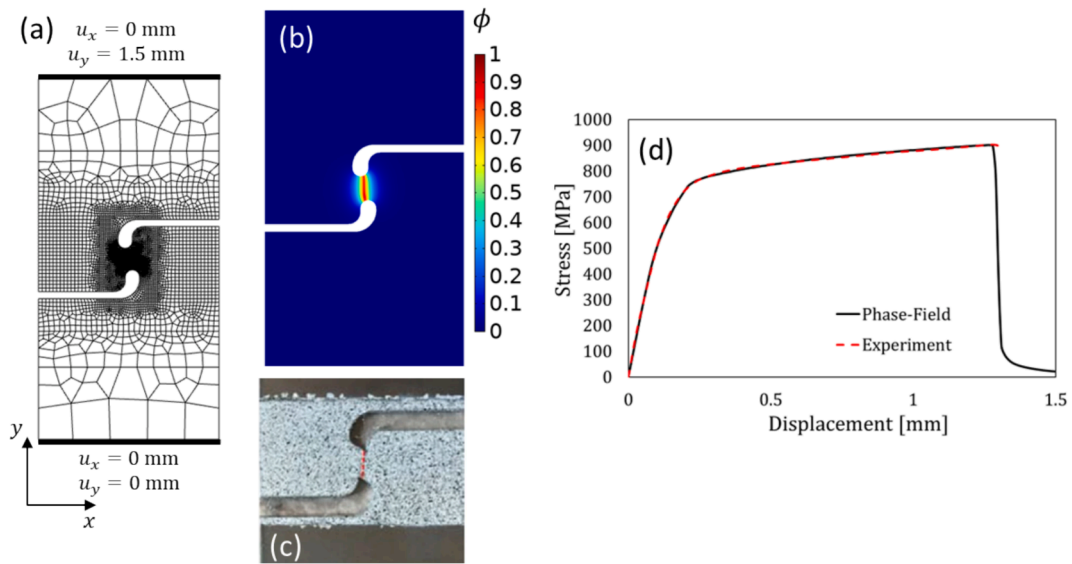

Fig. 12. (a) Mesh and boundary conditions. (b) Phase-field profile. (c) Experimental crack path. (d) Comparison of predicted and experimental stress-displacement response.

Table 4
Material and model properties for steel sheet.

Property	Value
Young's Modulus, E	210 GPa
Poisson Ratio, ν	0.3
Critical Stress, τ_c	1.4 GPa
Critical Energy Release Rate, G_c	60 N/mm
Length Scale, L	2 mm

Table 5
Plastic hardening curve for steel sheet.

Plastic Strain	Yield Stress
0	900 MPa
0.01	1200 MPa
0.02	1350 MPa
0.05	1360 MPa

in both quasi-brittle and ductile fracture. Furthermore, the mechanical response predictions were not particularly sensitive to the choice of the regularization length scale parameter. This represents an important feature of the model since the regularization length can be chosen as a numerical parameter which depends on mesh size as opposed to a material parameter.

Author statement

We declare that this manuscript entitled "Length Scale Insensitive Phase-Field Fracture Methodology for Brittle and Ductile Materials" is original, has not been published before and is not currently being considered for publication elsewhere.

CRediT authorship contribution statement

William Huber: Writing – original draft, Visualization, Validation, Software, Methodology, Investigation, Formal analysis, Data curation, Conceptualization. **Mohsen Asle Zaeem:** Writing – review & editing, Supervision, Project administration, Methodology, Investigation, Funding acquisition, Conceptualization.

Declaration of competing interest

The authors declare that they have no known competing financial interests or personal relationships that could have appeared to influence the work reported in this paper.

Data availability

Data will be made available on request.

Appendix A. . Variational framework for models A, B and D

Here we present details on the variational structure of the models A, B and D, despite the variationally inconsistent final forms that we have implemented. We begin with the assumption that the temperature of our material in question is spatially and temporally constant. The Clausius-Duhem inequality [48] can then be written as:

$$\int_\Omega (\boldsymbol{\sigma} : \dot{\boldsymbol{\varepsilon}} - \dot{\psi}) d\Omega \geq 0 \tag{A1}$$

where $\dot{x}$ denotes a time derivative. ψ is the Helmholtz energy density which is given for the general elasto-plastic case as:

$$\psi = \psi^e(\boldsymbol{\varepsilon}, \boldsymbol{\varepsilon}^p, \phi) + \psi^p(\alpha, \phi) + \psi^f(\phi) \tag{A2}$$

where ψ^e is the elastic strain energy, ψ^p is the plastic energy density, and $\psi^f(\phi)$ is the crack energy density which can be of the AT1 or AT2 type. By inserting (A2) into (A1) we arrive at the expression:

$$\int_\Omega - \left[\frac{\partial \psi^e}{\partial \boldsymbol{\varepsilon}^p} : \dot{\boldsymbol{\varepsilon}}^p + \frac{\partial \psi^p}{\partial \alpha} \dot{\alpha} + \left(\frac{\partial \psi^e}{\partial \phi} + \frac{\partial \psi^p}{\partial \phi} + \frac{\partial \psi^f}{\partial \phi} \right) \dot{\phi} + \frac{\partial \psi^f}{\partial \nabla \phi} \bullet \nabla \dot{\phi} \right] d\Omega \geq 0 \tag{A3}$$

We also define the following dissipative forces:

$$\chi^p = \frac{\partial \psi^e}{\partial \boldsymbol{\varepsilon}^p}, \ r^p = \frac{\partial \psi^p}{\partial \alpha} \tag{A4}$$

$$\chi^f = \frac{\partial \psi^e}{\partial \phi} + \frac{\partial \psi^p}{\partial \phi}, \ r^f = \frac{\delta \psi^f}{\delta \phi} = \frac{\partial \psi^f}{\partial \phi} - \nabla \bullet \frac{\partial \psi^f}{\partial \nabla \phi} \tag{A5}$$

With the additive decomposition of strain, $\chi^p = -\sigma$. Considering a plastic threshold, Φ^p, an elastic domain for the material is defined as:

$$\mathbb{E}_p = \{\chi^p, r^p | \Phi^p(\chi^p, r^p) \leq 0\} \tag{A6}$$

And an intact domain with a fracture threshold, Φ^f, is defined as:

$$\mathbb{E}_f = \{\chi^f, r^f | \Phi^f(\chi^f, r^f) \leq 0\} \tag{A7}$$

With the principle of maximum dissipation, we write the (local) dissipation potential as:

$$D = \sup_{(\chi^p, r^p) \in \mathbb{E}_p, (\chi^f, r^f) \in \mathbb{E}_f} \left[- \left(\chi^p : \dot{\boldsymbol{\varepsilon}}^p + r^p \dot{\alpha} + (\chi^f + r^f) \dot{\phi} \right) \right] \tag{A8}$$

To simplify the notation, we will also define:

$$\chi = \{\chi^p, r^p, \chi^f, r^f\} \tag{A9}$$

Which can be rewritten with Lagrange multipliers, λ^p and λ^f, as:

$$D = \sup_{(\chi, \lambda^p \geq 0, \lambda^f \geq 0)} \left[- \left(\chi^p : \dot{\boldsymbol{\varepsilon}}^p + r^p \dot{\alpha} + (\chi^f + r^f) \dot{\phi} \right) - \lambda^p \Phi^p(\chi^p, r^p) - \lambda^f \Phi^f(\chi^f, r^f) \right] \tag{A10}$$

Stationarity of the dissipation potential results in the following Euler equations:

$$\delta_{\chi^p} D = -\dot{\boldsymbol{\varepsilon}}^p - \lambda^p \frac{\partial \Phi^p}{\partial \chi^p} = 0 \tag{A11}$$

$$\delta_{r^p} D = -\dot{\alpha} - \lambda^p \frac{\partial \Phi^p}{\partial r^p} = 0 \tag{A12}$$

$$\delta_{\chi^f} D = -\dot{\phi} - \lambda^f \frac{\partial \Phi^f}{\partial \chi^f} = 0 \tag{A13}$$

$$\delta_{r^f} D = -\dot{\phi} - \lambda^f \frac{\partial \Phi^f}{\partial r^f} = 0 \tag{A14}$$

Along with the Karush-Kuhn-Tucker conditions:

$$\lambda^p \geq 0, \Phi^p \leq 0, \lambda^p \Phi^p = 0 \tag{A15}$$

$$\lambda^f \geq 0, \Phi^f \leq 0, \lambda^f \Phi^f = 0 \tag{A16}$$

From equation (A12), λ^p can be written as:

$$\lambda^p = -\left(\frac{\partial \Phi^p}{\partial r^p}\right)^{-1} \dot{\alpha} \tag{A17}$$

With (A17) inserted into (A11), $\dot{\varepsilon}^p$ can be written as:

$$\dot{\varepsilon}^p = \left(-\frac{\partial \Phi^p}{\partial r^p}\right)^{-1} \dot{\alpha} \frac{\partial \Phi^p}{\partial \chi^p} \tag{A18}$$

where α can now be identified as equivalent plastic strain. Insertion of (A18) into (A3) implies that the plastic threshold (or yield function) must be of the form:

$$\Phi^p = -\chi^p : \frac{\partial \Phi^p}{\partial \chi^p} \left(-\frac{\partial \Phi^p}{\partial r^p}\right)^{-1} - r^p \tag{A19}$$

where $\frac{\partial \Phi^p}{\partial \chi^p}$ can be identified as the (negative) flow direction of plastic deformation. Furthermore, it is now apparent that $\lambda^p = \dot{\alpha}$. Specifying to the von Mises yield function, (A19) can be written as:

$$\Phi^p = \sqrt{3J_2(\boldsymbol{\sigma})} - r^p = \sqrt{3J_2(\boldsymbol{\sigma})} - \sigma_y(\alpha) \tag{A20}$$

Meanwhile, (A13) and (A14) imply that:

$$\frac{\partial \Phi^f}{\partial \chi^f} = \frac{\partial \Phi^f}{\partial r^f} \tag{A20}$$

And thus, with (A3), the fracture yield function must be:

$$\Phi^f = -\chi^f - r^f \tag{A21}$$

With the prior relations established, we can now consider the variational principle of the elasto-plastic-fracture problem. The potential considered is:

$$\Pi = \int_\Omega (\dot{\psi} + D) d\Omega - \int_S t\dot{u} dS \tag{A22}$$

To simplify notation, we define:

$$\boldsymbol{\eta} = \{\dot{\boldsymbol{u}}, \dot{\alpha}, \dot{\phi}\} \tag{A23}$$

The evolution of the state variables can be determined from the variational principle discussed in [49]:

$$\{\boldsymbol{\eta}, \chi, \lambda^p, \lambda^f\} = \mathrm{Arg}\left\{ \inf_{\boldsymbol{\eta}} \sup_{\chi, \lambda^p \geq 0, \lambda^f \geq 0} (\Pi) \right\} \tag{A24}$$

Which yields the Euler-Lagrange equations:

$$\nabla \bullet \boldsymbol{\sigma} = 0 \tag{A25}$$

$$\Phi^p = \sqrt{3J_2(\boldsymbol{\sigma})} - r^p \leq 0 \tag{A26}$$

$$\dot{\alpha} \geq 0, \dot{\alpha}\Phi^p = 0 \tag{27}$$

$$\Phi^f = -\left(\frac{\partial \psi^e}{\partial \phi} + \frac{\partial \psi^p}{\partial \phi}\right) - \left(\frac{\partial \psi^f}{\partial \phi} - \nabla \bullet \frac{\partial \psi^f}{\partial \nabla \phi}\right) \leq 0 \tag{A28}$$

$$\dot{\phi} \geq 0, \dot{\phi}\Phi^f = 0 \tag{A29}$$

Setting $\psi^p = 0$ with the specific constitutive choices in equations (8)-(11) eliminates (A26) and (A27) and yields model A, while the specific constitutive choices in equations (19)-(23) yield model B. Model D is recovered with $\psi^p \neq 0$ and the constitutive choices in equations (48) – (55).

Appendix B. . Variational framework for model C

Here we present details on the variational structure of model C. The Helmholtz energy density is given as:

$$\psi = \psi^e(\boldsymbol{\varepsilon}, \gamma) + \psi^\gamma(\gamma, \phi) + \psi^f(\phi) \tag{B1}$$

$$\psi^\gamma(\gamma, \phi) = g_q(\phi)\psi_c\gamma \tag{B2}$$

$$\psi^f(\phi) = \psi^{AT2}(\phi) \tag{B3}$$

where ψ^e is the elastic strain energy and ψ^γ is the damage energy. By inserting (B1) into (A1) we arrive at the expression:

$$\int_\Omega - \left[\left(\frac{\partial \psi^e}{\partial \gamma} + \frac{\partial \psi^\gamma}{\partial \gamma} \right) \dot{\gamma} + \left(\frac{\partial \psi^\gamma}{\partial \phi} + \frac{\partial \psi^f}{\partial \phi} \right) \dot{\phi} + \frac{\partial \psi^f}{\partial \nabla \phi} \bullet \nabla \dot{\phi} \right] d\Omega \geq 0 \tag{B4}$$

We also define the following dissipative forces:

$$\chi^\gamma = \frac{\partial \psi^e}{\partial \gamma}, \ r^\gamma = \frac{\partial \psi^\gamma}{\partial \gamma} \tag{B5}$$

$$\chi^f = \frac{\partial \psi^\gamma}{\partial \phi}, \ r^f = \frac{\delta \psi^f}{\delta \phi} = \frac{\partial \psi^f}{\partial \phi} - \nabla \bullet \frac{\partial \psi^f}{\partial \nabla \phi} \tag{B6}$$

Considering a threshold for γ, Φ^γ, an elastic domain for the material is defined as:

$$\mathbb{E}_\gamma = \{ \chi^\gamma, r^\gamma : \Phi^\gamma(\chi^\gamma, r^\gamma) \leq 0 \} \tag{B7}$$

And an intact domain with a fracture threshold, Φ^f, is defined as:

$$\mathbb{E}_f = \{ \chi^f, r^f : \Phi^f(\chi^f, r^f) \leq 0 \} \tag{B8}$$

With the principle of maximum dissipation, we write the (local) dissipation potential as:

$$D = \sup_{(\chi^\gamma, r^\gamma) \in \mathbb{E}_\gamma, (\chi^f, r^f) \in \mathbb{E}_f} \left[- \left((\chi^\gamma + r^\gamma)\dot{\gamma} + (\chi^f + r^f)\dot{\phi} \right) \right] \tag{B9}$$

To simplify the notation, we will also define:

$$\boldsymbol{\chi} = \{ \chi^\gamma, r^\gamma, \chi^f, r^f \} \tag{B10}$$

Which can be rewritten with Lagrange multipliers, λ^γ and λ^f, as:

$$D = \sup_{(\boldsymbol{\chi}, \lambda^\gamma \geq 0, \lambda^f \geq 0)} \left[- \left((\chi^\gamma + r^\gamma)\dot{\gamma} + (\chi^f + r^f)\dot{\phi} \right) - \lambda^\gamma \Phi^\gamma(\chi^\gamma, r^\gamma) - \lambda^f \Phi^f(\chi^f, r^f) \right] \tag{B11}$$

Stationarity of the dissipation potential results in the following Euler-Lagrange equations:

$$\delta_{\chi^\gamma} D = - \dot{\gamma} - \lambda^\gamma \frac{\partial \Phi^\gamma}{\partial \chi^\gamma} = 0 \tag{B12}$$

$$\delta_{r^\gamma} D = - \dot{\gamma} - \lambda^\gamma \frac{\partial \Phi^\gamma}{\partial r^\gamma} = 0 \tag{B13}$$

$$\delta_{\chi^f} D = - \dot{\phi} - \lambda^f \frac{\partial \Phi^f}{\partial \chi^f} = 0 \tag{B14}$$

$$\delta_{r^f} D = - \dot{\phi} - \lambda^f \frac{\partial \Phi^f}{\partial r^f} = 0 \tag{B15}$$

Along with the Karush-Kuhn-Tucker conditions:

$$\lambda^\gamma \geq 0, \Phi^\gamma \leq 0, \lambda^\gamma \Phi^\gamma = 0 \tag{B16}$$

$$\lambda^f \geq 0, \Phi^f \leq 0, \lambda^f \Phi^f = 0 \tag{B17}$$

(B12-B15) imply that:

$$\frac{\partial \Phi^\gamma}{\partial \chi^\gamma} = \frac{\partial \Phi^\gamma}{\partial r^\gamma} \tag{B18}$$

$$\frac{\partial \Phi^f}{\partial \chi^f} = \frac{\partial \Phi^f}{\partial r^f} \tag{B19}$$

Therefore, with (B4), the damage yield function, Φ^γ, must be:

$$\Phi^\gamma = - \chi^\gamma - r^\gamma \tag{B20}$$

And the fracture yield function, Φ^f, must be:

$$\Phi^f = - \chi^f - r^f \tag{B21}$$

(B12-B15) then imply that $\lambda^\gamma = \dot{\gamma}$ and $\lambda^f = \dot{\phi}$. The potential of the quasi-brittle fracture problem is determined given by:

$$\Pi = \int_\Omega (\dot{\psi} + D) d\Omega - \int_S t \dot{u} dS \tag{B22}$$

To simplify notation, we define:

$$\eta = \{\dot{\boldsymbol{u}}, \dot{\gamma}, \dot{\phi}\} \tag{B23}$$

The evolution of the state variables can be determined from the variational principle:

$$\{\eta, \chi, \lambda^p, \lambda^s, \lambda^f\} = \text{Arg}\left\{\inf_{\eta} \sup_{\chi, \lambda^\gamma \geq 0, \lambda^f \geq 0}(\Pi)\right\} \tag{B24}$$

Which yields the following Euler-Lagrange equations in Ω:

$$\nabla \bullet \boldsymbol{\sigma} = 0 \tag{25}$$

$$\Phi^\gamma = -\frac{\partial \psi^e}{\partial \gamma} - \frac{\partial \psi^\gamma}{\partial \gamma} \leq 0, \dot{\gamma} \geq 0, \dot{\gamma}\Phi^\gamma = 0 \tag{B26}$$

$$\Phi^f = -\frac{\partial \psi^\gamma}{\partial \phi} - \frac{\partial \psi^f}{\partial \phi} - \nabla \bullet \frac{\partial \psi^f}{\partial \nabla \phi} \leq 0, \dot{\phi} \geq 0, \dot{\phi}\Phi^f = 0 \tag{B27}$$

Appendix C. . Variational framework for model E

Here, we present details on the variational structure of model E. The Helmholtz energy density is given as:

$$\psi = \psi^e(\boldsymbol{\varepsilon}, \boldsymbol{\varepsilon}^p, \boldsymbol{\varepsilon}^s) + \psi^p(\alpha) + \psi^s(s, \phi) + \psi^f(\phi) \tag{C1}$$

$$\psi^s(s, \phi) = g_q(\phi)\tau_c s \tag{C2}$$

$$\psi^f(\phi) = \psi^{AT2}(\phi) \tag{C3}$$

ψ^e is the elastic strain energy, ψ^p is the plastic energy density, ψ^s is the sliding energy density and ψ^f is the crack energy density. By inserting (C1) into (A1) we arrive at the expression:

$$\int_\Omega -\left[\frac{\partial \psi^e}{\partial \boldsymbol{\varepsilon}^p} : \dot{\boldsymbol{\varepsilon}}^p + \frac{\partial \psi^e}{\partial \boldsymbol{\varepsilon}^s} : \dot{\boldsymbol{\varepsilon}}^s + \frac{\partial \psi^p}{\partial \alpha}\dot{\alpha} + \frac{\partial \psi^s}{\partial s}\dot{s} + \left(\frac{\partial \psi^s}{\partial \phi} + \frac{\partial \psi^f}{\partial \phi}\right)\dot{\phi} + \frac{\partial \psi^f}{\partial \nabla \phi} \bullet \nabla\dot{\phi}\right]d\Omega \geq 0 \tag{C4}$$

We also define the following dissipative forces:

$$\chi^p = \frac{\partial \psi^e}{\partial \boldsymbol{\varepsilon}^p}, \ r^p = \frac{\partial \psi^p}{\partial \alpha} \tag{C5}$$

$$\chi^s = \frac{\partial \psi^e}{\partial \boldsymbol{\varepsilon}^s}, \ r^s = \frac{\partial \psi^s}{\partial s} \tag{C6}$$

$$\chi^f = \frac{\partial \psi^s}{\partial \phi}, \ r^f = \frac{\delta \psi^f}{\delta \phi} = \frac{\partial \psi^f}{\partial \phi} - \nabla \bullet \frac{\partial \psi^f}{\partial \nabla \phi} \tag{C7}$$

With the additive decomposition of strain, $\chi^p = \chi^s = -\boldsymbol{\sigma}$. Considering a plastic threshold, Φ^p, an elastic domain for the material is defined as:

$$\mathbb{E}_p = \{\chi^p, r^p : \Phi^p(\chi^p, r^p) \leq 0\} \tag{C8}$$

Meanwhile, a sliding threshold, Φ^s, is defined as:

$$\mathbb{E}_s = \{\chi^s, r^s : \Phi^s(\chi^s, r^s) \leq 0\} \tag{C9}$$

And an intact domain with a fracture threshold, Φ^f, is defined as:

$$\mathbb{E}_f = \{\chi^f, r^f : \Phi^f(\chi^f, r^f) \leq 0\} \tag{C10}$$

With the principle of maximum dissipation, we write the (local) dissipation potential as:

$$D = \sup_{(\chi^p, r^p) \in \mathbb{E}_p, (\chi^s, r^s) \in \mathbb{E}_s, (\chi^f, r^f) \in \mathbb{E}_f}\left[-\left(\chi^p : \dot{\boldsymbol{\varepsilon}}^p + r^p\dot{\alpha} + \chi^s : \dot{\boldsymbol{\varepsilon}}^s + r^s\dot{s} + (\chi^f + r^f)\dot{\phi}\right)\right] \tag{C11}$$

To simplify the notation, we will define:

$$\chi = \{\chi^p, r^p, \chi^s, r^s, \chi^f, r^f\} \tag{C12}$$

D can be rewritten with Lagrange multipliers, λ^p, λ^s and λ^f, as:

$$D = \sup_{(\chi, \lambda^p \geq 0, \lambda^s \geq 0, \lambda^f \geq 0)}\left[-\left(\chi^p : \dot{\boldsymbol{\varepsilon}}^p + r^p\dot{\alpha} + \chi^s : \dot{\boldsymbol{\varepsilon}}^s + r^s\dot{s} + (\chi^f + r^f)\dot{\phi}\right) - \lambda^p\Phi^p(\chi^p, r^p) - \lambda^s\Phi^s(\chi^s, r^s) - \lambda^f\Phi^f(\chi^f, r^f)\right] \tag{C13}$$

Stationarity of the dissipation potential results in the following Euler-Lagrange equations:

$$\delta_{\chi^p}D = -\dot{\boldsymbol{\varepsilon}}^p - \lambda^p\frac{\partial \Phi^p}{\partial \chi^p} = 0 \tag{C14}$$

$$\delta_{r^p} D = -\dot{\alpha} - \lambda^p \frac{\partial \Phi^p}{\partial r^p} = 0 \tag{C15}$$

$$\delta_{\chi^s} D = -\dot{\varepsilon}^s - \lambda^s \frac{\partial \Phi^s}{\partial \chi^s} = 0 \tag{C16}$$

$$\delta_{r^s} D = -\dot{s} - \lambda^s \frac{\partial \Phi^s}{\partial r^s} = 0 \tag{C17}$$

$$\delta_{\chi^f} D = -\dot{\phi} - \lambda^f \frac{\partial \Phi^f}{\partial \chi^f} = 0 \tag{C18}$$

$$\delta_{r^f} D = -\dot{\phi} - \lambda^f \frac{\partial \Phi^f}{\partial r^f} = 0 \tag{C19}$$

Along with the Karush-Kuhn-Tucker conditions:

$$\lambda^p \geq 0, \Phi^p \leq 0, \lambda^p \Phi^p = 0 \tag{C20}$$

$$\lambda^s \geq 0, \Phi^s \leq 0, \lambda^s \Phi^s = 0 \tag{C21}$$

$$\lambda^f \geq 0, \Phi^f \leq 0, \lambda^f \Phi^f = 0 \tag{C22}$$

From equation (C15), λ^p can be written as:

$$\lambda^p = -\left(\frac{\partial \Phi^p}{\partial r^p}\right)^{-1} \dot{\alpha} \tag{C23}$$

And λ^s can similarly be written as:

$$\lambda^s = -\left(\frac{\partial \Phi^s}{\partial r^s}\right)^{-1} \dot{s} \tag{C24}$$

With (C23) inserted into (C14), $\dot{\varepsilon}^p$ can be written as:

$$\dot{\varepsilon}^p = \left(-\frac{\partial \Phi^p}{\partial r^p}\right)^{-1} \dot{\alpha} \frac{\partial \Phi^p}{\partial \chi^p} \tag{C25}$$

where α can now be identified as equivalent plastic strain. Insertion of (C25) into (C4) implies that the plastic threshold (or yield function) must be of the form:

$$\Phi^p = -\chi^p : \frac{\partial \Phi^p}{\partial \chi^p}\left(-\frac{\partial \Phi^p}{\partial r^p}\right)^{-1} - r^p \tag{C26}$$

where $\frac{\partial \Phi^p}{\partial \chi^p}$ can be identified as the (negative) flow direction of plastic deformation. Following a similar procedure, the sliding threshold is:

$$\Phi^s = -\chi^s : \frac{\partial \Phi^s}{\partial \chi^s}\left(-\frac{\partial \Phi^s}{\partial r^s}\right)^{-1} - r^s \tag{C27}$$

The lagrange multipliers λ^p and λ^s can now be interpreted as:

$$\lambda^p = \dot{\alpha} \tag{C28}$$

$$\lambda^s = \dot{s} \tag{C29}$$

Specifying to the von Mises yield function for both plasticity and sliding, (C26) can be written as:

$$\Phi^p = \sqrt{3J_2(\boldsymbol{\sigma})} - r^p \tag{C30}$$

And (C27) can be written as:

$$\Phi^s = \sqrt{3J_2(\boldsymbol{\sigma})} - r^s \tag{C31}$$

Meanwhile, (C18) and (C19) imply that:

$$\frac{\partial \Phi^f}{\partial \chi^f} = \frac{\partial \Phi^f}{\partial r^f} \tag{C32}$$

And thus, with (C4), the fracture yield function must be:

$$\Phi^f = -\chi^f - r^f \tag{C33}$$

(C18) and (C19) then imply that $\lambda^f = \dot{\phi}$. With the prior relations established, we can now consider the variational principle of the elasto-plastic-fracture problem. Furthermore, to simplify notation, we define:

$$\eta = \{\dot{u}, \dot{\alpha}, \dot{s}, \dot{\phi}\} \tag{C34}$$

The potential considered is given by:

$$\Pi = \int_\Omega (\dot\psi + D)d\Omega - \int_S t\dot u \, dS \tag{C35}$$

The evolution of the state variables can be determined from the variational principle discussed in [49]:

$$\{\eta, \chi, \lambda^p, \lambda^s, \lambda^f\} = \text{Arg}\left\{\inf_{\eta} \sup_{\chi, \lambda^p \geq 0, \lambda^s \geq 0, \lambda^f \geq 0} (\Pi)\right\} \tag{C36}$$

Which yields the following (non-trivial) Euler-Lagrange equations in Ω:

$$\nabla \bullet \boldsymbol{\sigma} = 0 \tag{C37}$$

$$\Phi^p = \sqrt{3J_2(\boldsymbol{\sigma})} - r^p \leq 0, \ \dot\alpha \geq 0, \dot\alpha\Phi^p = 0 \tag{C38}$$

$$\Phi^s = \sqrt{3J_2(\boldsymbol{\sigma})} - r^s \leq 0, \ \dot s \geq 0, \dot s\Phi^s = 0 \tag{C39}$$

$$\Phi^f = -\left(\frac{\partial\psi^e}{\partial\phi} + \frac{\partial\psi^p}{\partial\phi}\right) - \left(\frac{\partial\psi^f}{\partial\phi} - \nabla \bullet \frac{\partial\psi^f}{\partial\nabla\phi}\right) \leq 0, \dot\phi \geq 0, \dot\phi\Phi^f = 0 \tag{C40}$$

References

[1] A. A. Griffith. (1921) "VI. The phenomena of rupture and flow in solids," *Philosophical transactions of the royal society of london. Series A, containing papers of a mathematical or physical character,* vol. 221, no. 582-593, pp. 163-198.

[2] G. R. Irwin. (1957) "Analysis of stresses and strains near the end of a crack traversing a plate,".

[3] N. Moës, J. Dolbow, T. Belytschko, A finite element method for crack growth without remeshing, Int. J. Numer. Meth. Eng. 46 (1) (1999) 131–150.

[4] D. Uribe-Suárez, P.-O. Bouchard, M. Delbo, D. Pino-Muñoz, Numerical modeling of crack propagation with dynamic insertion of cohesive elements, Eng. Fract. Mech. 227 (2020) 106918.

[5] R.H. Peerlings, R. de Borst, W. Brekelmans, M.G. Geers, Gradient-enhanced damage modelling of concrete fracture, Mechanics of Cohesive-Frictional Materials: An Int. J. Experiments, Modelling and Computation of Materials and Structures 3 (4) (1998) 323–342.

[6] Z.P. Bazant, J. Planas, Fracture and size effect in concrete and other quasibrittle materials, Routledge, 2019.

[7] G.A. Francfort, J.-J. Marigo, Revisiting brittle fracture as an energy minimization problem, J. Mech. Phys. Solids 46 (8) (1998) 1319–1342.

[8] B. Bourdin, G.A. Francfort, J.-J. Marigo, N*umerical experiments in revisited brittle fracture*, J. Mech. Phys. Solids 48 (4) (2000) 797–826.

[9] B. Bourdin, G.A. Francfort, J.-J. Marigo, The variational approach to fracture, J. Elast. 91 (1–3) (2008) 5–148.

[10] W. Huber, M. Asle Zaeem, A mixed mode phase-field model of ductile fracture, J. Mech. Phys. Solids 171 (2023) 105123.

[11] M. Dittmann, F. Aldakheel, J. Schulte, P. Wriggers, C. Hesch, Variational phase-field formulation of non-linear ductile fracture, Comp. Methods in Appl. Mechanics and Eng. 342 (2018) 71–94, https://doi.org/10.1016/j.cma.2018.07.029.

[12] B. Yin, M. Kaliske, Fracture simulation of viscoelastic polymers by the phase-field method, Comput. Mech. 65 (2) (2020) 293–309.

[13] A. Emdadi, W.G. Fahrenholtz, G.E. Hilmas, M. Asle Zaeem, A modified phase-field model for quantitative simulation of crack propagation in single-phase and multi-phase materials, Eng. Fract. Mech. 200 (2018) 339–354.

[14] A. Mesgarnejad, B. Bourdin, M. Khonsari, Validation simulations for the variational approach to fracture, Comput. Methods Appl. Mech. Eng. 290 (2015) 420–437.

[15] E. Lorentz, S. Cuvilliez, K. Kazymyrenko, Convergence of a gradient damage model toward a cohesive zone model, Comptes Rendus Mécanique 339 (1) (2011) 20–26.

[16] J.-Y. Wu, A unified phase-field theory for the mechanics of damage and quasi-brittle failure, J. Mech. Phys. Solids 103 (2017) 72–99.

[17] R.J. Geelen, Y. Liu, T. Hu, M.R. Tupek, J.E. Dolbow, A phase-field formulation for dynamic cohesive fracture, Comput. Methods Appl. Mech. Eng. 348 (2019) 680–711.

[18] X. Zhuang, S. Zhou, G. Huynh, P. Areias, T. Rabczuk, Phase field modeling and computer implementation: a review, Eng. Fract. Mech. 262 (2022) 108234.

[19] T. Gerasimov, L. De Lorenzis, On penalization in variational phase-field models of brittle fracture, Comput. Methods Appl. Mech. Eng. 354 (2019) 990–1026.

[20] T. Heister, M.F. Wheeler, T. Wick, A primal-dual active set method and predictor-corrector mesh adaptivity for computing fracture propagation using a phase-field approach, Comput. Methods Appl. Mech. Eng. 290 (2015) 466–495.

[21] M.F. Wheeler, T. Wick, W. Wollner, An augmented-Lagrangian method for the phase-field approach for pressurized fractures, Comput. Methods Appl. Mech. Eng. 271 (2014) 69–85.

[22] C. Li, J. Fang, C. Wu, G. Sun, G. Steven, Q. Li, Phase field fracture in elasto-plastic solids: Incorporating phenomenological failure criteria for ductile materials, Comput. Methods Appl. Mech. Eng. 391 (2022) 114580.

[23] J. Han, S. Matsubara, S. Moriguchi, K. Terada, Variational crack phase-field model for ductile fracture with elastic and plastic damage variables, Comput. Methods Appl. Mech. Eng. 400 (2022) 115577.

[24] T. Hu, B. Talamini, A.J. Stershic, M.R. Tupek, J.E. Dolbow, A variational phase-field model for ductile fracture with coalescence dissipation, Comput. Mech. 68 (2) (2021) 311–335.

[25] J.-Y. Wu, V.P. Nguyen, C.T. Nguyen, D. Sutula, S. Sinaie, S.P. Bordas, Phase-field modeling of fracture, Adv. Appl. Mech. 53 (2020) 1–183.

[26] C. Miehe, M. Hofacker, F. Welschinger, A *phase field model for rate-independent crack propagation: robust algorithmic implementation based on operator splits*, Comput. Methods Appl. Mech. Eng. 199 (45–48) (2010) 2765–2778.

[27] L. De Lorenzis, C. Maurini, Nucleation under multi-axial loading in variational phase-field models of brittle fracture, Int. J. Fract. 237 (1–2) (2022) 61–81.

[28] X. Zhang, C. Vignes, S.W. Sloan, D. Sheng, Numerical evaluation of the phase-field model for brittle fracture with emphasis on the length scale, Comput. Mech. 59 (5) (2017) 737–752.

[29] T. Hu, J. Guilleminot, J.E. Dolbow, A phase-field model of fracture with frictionless contact and random fracture properties: application to thin-film fracture and soil desiccation, Comput. Methods Appl. Mech. Eng. 368 (2020) 113106.

[30] E. Lorentz, V. Godard, Gradient damage models: toward full-scale computations, Comput. Methods Appl. Mech. Eng. 200 (21–22) (2011) 1927–1944.

[31] J.-Y. Wu, Y. Huang, Comprehensive implementations of phase-field damage models in Abaqus, Theor. Appl. Fract. Mech. 106 (2020) 102440.

[32] F. Fei, J. Choo, Double-phase-field formulation for mixed-mode fracture in rocks, Comput. Methods Appl. Mech. Eng. 376 (2021) 113655.

[33] W.-X. Chen, J.-Y. Wu, Phase-field cohesive zone modeling of multi-physical fracture in solids and the open-source implementation in Comsol Multiphysics, Theor. Appl. Fract. Mech. 117 (2022) 103153.

[34] F. Fei, J. Choo, A phase-field model of frictional shear fracture in geologic materials, Comput. Methods Appl. Mech. Eng. 369 (2020) 113265.

[35] F. Fei, J. Choo, A phase-field method for modeling cracks with frictional contact, Int. J. Numer. Meth. Eng. 121 (4) (2020) 740–762.

[36] E.A. de Souza Neto, D. Peric, D.R. Owen, Computational methods for plasticity: theory and applications, John Wiley & Sons, 2011.

[37] R. Hill, A theory of the yielding and plastic flow of anisotropic metals, Proce. Royal Society of London. Series A. Mathematical and Physical Sci. 193 (1033) (1948) 281–297.

[38] Y. Bai, T. Wierzbicki, Application of extended Mohr-Coulomb criterion to ductile fracture, Int. J. Fract. 161 (1) (2010) 1–20.

[39] N. Singh, C. Verhoosel, R. De Borst, E. Van Brummelen, A fracture-controlled path-following technique for phase-field modeling of brittle fracture, Finite Elem. Anal. Des. 113 (2016) 14–29.

[40] C.V. Verhoosel, J.J. Remmers, M.A. Gutiérrez, A dissipation-based arc-length method for robust simulation of brittle and ductile failure, Int. J. Numer. Meth. Eng. 77 (9) (2009) 1290–1321.

[41] Z. Suo, S. Ho, and X. Gong. (1993) "Notch ductile-to-brittle transition due to localized inelastic band,".

[42] D.S. Dugdale, Yielding of steel sheets containing slits, J. Mech. Phys. Solids 8 (2) (1960) 100–104.

[43] A.H. Cottrell, Mechanics of fracture in large structures, Proc. R. Soc. Lond. A 285 (1400) (1965) 10–21.

[44] J. G. Rots. (1988) "Computational modeling of concrete fracture,".

[45] F. Khameneh, A. Abedini, C. Butcher, Lengthscale effects in optical strain measurement for fracture characterization in simple shear, Int. J. Fract. 232 (2021) 153–180.

[46] M. Ambati, T. Gerasimov, L. De Lorenzis, Phase-field modeling of ductile fracture, Comput. Mech. 55 (5) (2015) 1017–1040, https://doi.org/10.1007/s00466-015-1151-4.

[47] C. Kuhn, T. Noll, R. Müller, On phase field modeling of ductile fracture, GAMM-Mitteilungen 39 (1) (2016) 35–54.

[48] E.B. Tadmor, R.E. Miller, R.S. Elliott, Continuum mechanics and thermodynamics: from fundamental concepts to governing equations, Cambridge University Press, 2012.

[49] C. Miehe, A multi-field incremental variational framework for gradient-extended standard dissipative solids, J. Mech. Phys. Solids 59 (4) (2011) 898–923.